Surface & Coatings Technology 475 (2023) 130128

Contents lists available at ScienceDirect

Surface & Coatings Technology

journal homepage: www.elsevier.com/locate/surfcoat

Full Length Article

Diamond-Like Carbon (DLC) and AlCrN films onto Ti-6Al-4V substrates by Laser-Powder Bed Fusion (L-PBF): Effect of substrate heat treatment and surface finish

Emanuele Ghio [a], Giovanni Bolelli [b,c,d,*], Alessandro Bertè [e], Emanuela Cerri [a]

[a] Department of Engineering and Architecture, University of Parma, Via G. Usberti 181/A, 43124 Parma, Italy
[b] Department of Engineering "Enzo Ferrari", University of Modena e Reggio Emilia, Via Pietro Vivarelli 10/1, 41125 Modena, Italy
[c] InterMech MO.RE. Centro Interdipartimentale per la Ricerca Applicata e i Servizi nel Settore della Meccanica Avanzata e della Motoristica, University of Modena and Reggio Emilia, Via Pietro Vivarelli 2, 41125 Modena, Italy
[d] Consorzio Interuniversitario Nazionale per la Scienza e Tecnologia dei Materiali (INSTM), Local Unit: Università di Modena e Reggio Emilia, Via Pietro Vivarelli 10/1, 41125 Modena, Italy
[e] LAFER S.p.A., Strada Di Cortemaggiore 31, 29122 Piacenza, Italy

ARTICLE INFO

Keywords:
Diamond-like carbon (DLC)
Physical vapor deposition (PVD)
Plasma-enhanced chemical vapor deposition (PE-CVD)
Additive manufacturing
Sliding Wear
Titanium alloy

ABSTRACT

This paper focuses on the performance of thin-film coatings onto additively manufactured Ti-6Al-4V. Specifically, because metal parts obtained by laser-powder bed fusion (L-PBF) often require post-process heat treatments and surface finishing to meet end-user specifications, we studied how the resulting changes to mechanical strength and surface roughness affect the performance of films deposited by physical or plasma-enhanced chemical vapor deposition (PVD, PE-CVD). L-PBF Ti-6Al-4V substrates were heat-treated either below or above the β-transus and finished by grinding with different grit sizes, and then were coated with PVD AlCrN or a PE-CVD DLC-based film.

Scratch adhesion on harder surfaces treated below the β-transus was higher with both coating types, whilst the substrate finishing had a negligible effect. Conversely, in ball-on-disc sliding wear tests, substrate roughness had a dominant effect: rough surfaces always resulted in earlier cracking and delamination of the coatings. Substrate hardness had a minor effect only with the AlCrN film. Moreover, the DLC-based films, because of the low-friction conditions they establish through a graphitized tribofilm as well as their higher H/E ratio, survived severe contact conditions better than the stiffer AlCrN. The results were interpreted in the light of the plasticity indices of the coated systems and their tribochemical interactions.

1. Introduction

Additive manufacturing technologies are becoming increasingly widespread and have disparate applications e.g. in the aerospace and automotive industries; in the production of medical parts (scaffolds, prosthetic implants, etc.); for moulds, cores and inserts for the metal casting industry; as well as for the production of various consumer goods [1].

Titanium and its alloys, including the well-known Ti-6Al-4V composition, are among the materials most frequently studied and employed for many of those applications [2,3], due to their excellent strength-to-weight ratio, corrosion resistance, biocompatibility, etc. [4].

Their microstructure can be extensively tweaked through suitable heat-treatments, yielding a variety of grain sizes and morphologies, and a correspondingly wide range of achievable mechanical properties. For instance, quenching of a Ti-6Al-4V alloy after a solution treatment above the β-transus induces the formation of a metastable martensitic phase (α') by diffusionless transformation, resulting in high mechanical strength but also low toughness. Subsequent ageing gradually converts α'-martensite into an equilibrium α + β microstructure, which coarsens progressively as the treatment time and/or temperature increase, with a corresponding decrease of the yield and ultimate strength but a simultaneous increase of the elongation at fracture [5–7].

Additively manufactured Ti-6Al-4V alloys, and in particular those obtained by the laser-powder bed fusion (L-PBF) process, also known as selective laser melting (SLM), possess peculiar microstructures. As a

* Corresponding author at: Department of Engineering and Architecture, University of Parma, Via G. Usberti 181/A, 43124 Parma, Italy.
E-mail address: giovanni.bolelli@unimore.it (G. Bolelli).

https://doi.org/10.1016/j.surfcoat.2023.130128
Received 22 August 2023; Received in revised form 19 October 2023; Accepted 20 October 2023
Available online 23 October 2023

powder layer with a thickness of few tens of micrometres is melted and consolidated by a fast-moving laser, columnar β-grains grow epitaxially from the underlying layer, extending along the build direction [8–10], and develop acicular α'-martensite because the melt pool cools down very rapidly as it loses heat to the underlying solid [8,10], effectively inducing a quenching effect.

Thus, as-built L-PBF Ti-6Al-4V [2] is in a condition similar, though not identical, to a solution-annealed and quenched part [5]. It possesses high mechanical strength but insufficient elongation at fracture for most applications [11]. For this reason, L-PBF Ti-6Al-4V almost always needs a heat treatment to meet most specifications on mechanical properties [2,8].

The peculiar as-built microstructure of L-PBF Ti-6Al-4V enables innovative heat treatment procedures, departing from "standard" heat-treatments known for conventionally manufactured parts. Specifically, an L-PBF part can be directly aged below the β-transus to convert the as-built martensitic microstructure into a fine, acicular α-phase with correspondingly fine-grained β-phase along its boundaries. The material retains high mechanical strength though acquiring an acceptable elongation to fracture, and it also keeps the original, columnar morphology of the prior β-grains. On the other hand, when greater ductility is required, a heat-treatment above the β-transus re-crystallizes the material completely, erasing the memory of the columnar prior β-grains, and then, depending on the cooling rate, leads to a more or less coarse-grained α + β microstructure [11–13].

Modifying the mechanical strength of a component not only has obvious relevance for its performance under structural (static or cyclic) loads, but it also affects the mechanical support that the component offers to a coating [14,15].

This latter aspect is relevant because, in spite of their good mechanical strength, titanium and its alloys, including Ti-6Al-4V, have limited wear resistance [16]. There are multiple reasons for this behaviour [17]. Films formed by tribo-oxidation tend not to be particularly compact and protective, especially at low sliding speeds, and Ti alloys also have limited ability to work-harden [17–19]. In fact, deformation under sliding contact conditions tends to proceed inhomogeneously by adiabatic shear banding, which eventually leads to subsurface cracking and results in rather severe adhesion/delamination wear [18–20].

Thus, it is often necessary to protect Ti alloy parts by coatings or surface treatments in any application involving tribological contacts [16,21]. Among the many available options (plating, diffusion treatments, conversion treatments, anodizing or plasma electrolytic oxidation, etc.) [21], Physical and/or Plasma-Enhanced Chemical Vapor Deposition (PVD, PE-CVD) techniques are of particular interest. The hard layers deposited by PVD and/or PE-CVD provide excellent wear protection and, especially with Diamond-Like Carbon (DLC) films, reduce friction in the tribological coupling with most engineering counterparts [22]. Moreover, the low thickness (usually no more than few micrometres) of these coatings is compatible with the dimensional requirements of the precision parts that are often manufactured by L-PBF.

Films with a micrometre-scale thickness are "thin" from a mechanical point of view, because contact stress distributions under engineering conditions extend below the coating and affect the substrate as well. Therefore, as mentioned above, the load-carrying ability of the substrate plays a significant role on the integrity of the whole system [15,23]. A substrate whose hardness and/or elastic modulus are much lower than those of a thin-film coating induces contact stress concentrations in the film and along the film/substrate interface, which can cause the film to crack and spall off. Thus, although the heat-treatment condition of a L-PBF Ti-6Al-4V part is often dictated by the balance between strength and ductility needed for structural load-carrying requirements, it is important to determine how it affects the performance of thin-film coatings as well.

However, little information is available on whether and how diverse types of conventional and non-conventional heat treatments affect the performance of L-PBF Ti-alloy parts with PVD and/or PE-CVD coatings. In fact, even though some works showed that the deposition of thin-film coatings onto additively manufactured substrates is possible and yields fully satisfactory results, comparable to the performances that those films have on conventionally manufactured parts [24–32], only very few papers examined how the heat treatment condition of an additively manufactured part affects the performance of the coated system. Li et al. [33] showed that an as-built L-PBF Ti-6Al-4V substrate with martensitic (α') microstructure provided better mechanical support to a PVD TiN coating than did a machined part with α + β microstructure, though the heat-treatment condition of the latter was not disclosed in the paper. This result, however, might be of limited practical relevance due to the above-mentioned brittleness of an as-built, martensitic part.

Additionally, another important feature of additive manufacturing processes with respect to the deposition of thin-film coatings is their surface roughness. Additive manufacturing, including L-PBF, produces rough surfaces, with features such as interlayer steps, unmelted particles, "balling" effects, shrinkage cavities, etc. [34–37], so that Ra values around or above 10 μm are common.

This roughness is incompatible with a thin-film coating, because contact stress concentrations caused by the asperities of a rough underlying surface can result in premature cracking and detachment of a thin film [38]. There is a wide range of options available for surface finishing of additively manufactured parts [39,40], producing different surface textures on the processed part. However, there are few studies on how the surface finishing of additively manufactured (in particular, L-PBF) parts affects the performance of a thin-film coating. Some of the present authors studied the performance of DLC-based films deposited onto L-PBF AlSi10Mg alloys with different surface finishes achieved by mechanical processes (grinding, polishing, or shot-peening) [41]. The sliding wear rate of the coating against a sintered Al_2O_3 ball varied non-monotonically with the substrate roughness. Wear loss was minimum at Sq ~ 0.5–1.5 μm and increased at both lower and higher roughness values [41]. Interestingly, Vella et al. reported a good sliding wear response of a nitride-based PVD coating on a shot-peened L-PBF surface with Sa ~ 1.5 μm, which is not too far from the range mentioned above [42]. Tillmann et al. reported that the open porosity on the polished surface of 316 L substrates obtained by binder jetting and sintering did not have much of a detrimental effect on the adhesion of a DLC-based coating [28], but, on the other hand, they also found that DLC-based coatings adhered a bit worse to a polished L-PBF 36NiCrMo16 substrate with Ra ≈ 0.008 μm than to an identically finished, wrought part with Ra ≈ 0.003 μm [43].

Thus, the issues of both the heat-treatment and surface finishing effects remain open and are worthy of further investigation. To this end, in this work we chose L-PBF Ti-6Al-4V parts subjected to two different heat-treatment procedures, respectively below and above the β-transus. The microstructure and mechanical properties (yield and ultimate tensile strength, elongation at fracture, hardness) of these materials had been thoroughly investigated in our previous work [44]. The parts were subjected to two different finishing procedures: manual grinding with SiC-based sandpaper, which resulted in a rougher surface, or grinding followed by chemical-mechanical polishing, yielding a smoother finish. Finally, substrates with each of the four heat treatment/finishing combinations were coated with either a PE-CVD DLC-based film or a PVD AlCrN film. The former is frequently employed to combine hardness and wear resistance with low friction [22], whilst the latter is a typical example of a very hard and stiff nitride-based film used primarily for wear protection [45–48], including on Ti-6Al-4V substrates [47]. The adhesion strength and sliding wear behaviour of all systems were analysed, and comparisons were also made to literature data for conventionally machined Ti-6Al-4V parts with analogous coating types tested under comparable conditions.

Table 1
Summary of the mechanical properties of the Ti64 substrates in different heat-treatment conditions, from [44].

Heat treatment conditions	Yield strength [MPa]	Ultimate tensile strength [MPa]	Elongation to fracture (%)	$HV_{0.5}$*
740 °C / 130 min	960 ± 10	1025 ± 10	11.05 ± 0.49	370 ± 6
1050 °C / 60 min	818 ± 7	918 ± 7	12.75 ± 1.01	341 ± 3

* Averaged from the data in [44] over all orientations.

Table 2
The main roughness parameters for "rough" and "smooth" substrates.

	"Rough" substrates	"Smooth" substrates
Sa [μm]	2.004 ± 0.215	0.179 ± 0.095
Sq [μm]	2.392 ± 0.305	0.250 ± 0.104
Sz [μm]	22.10 ± 2.10	7.99 ± 0.64
Ssk	−0.185 ± 0.004	−0.200 ± 0.009
Sku	2.371 ± 0.206	4.254 ± 0.363
Spc [mm^{-1}]	520.6 ± 18.5	119.1 ± 7.3

2. Experimental

2.1. Preparation of the substrates

Samples were manufactured by Laser-Powder Bed Fusion (L-PBF) using a Ti-6Al-4V Extra-Low Interstitials (ELI) feedstock powder, hereafter briefly designated as "Ti64". Specifically, we manufactured Ti64 bars which were horizontally laser-power bed fused with respect to the build platform ($0°_{XY}$ direction in [44]) under processing conditions previously described in [44].

Bars were then removed from the platform after a heat treatment. Indeed, as explained in the Introduction, L-PBF Ti64 in the as-manufactured condition would be too brittle for any practical application and would probably crack even during separation from the build platform. In our previous works, we investigated the effects of heat-treatments at temperatures both below and above the β-transus [44,49]. Thus, in order to assess whether the different mechanical properties caused by these two types of treatments also have an effect on the performance of thin-film coatings, two heat treatment conditions were chosen: 740 °C for 130 min (i.e. below the β-transus) and 1050 °C for 60 min (above the β-transus). Full experimental details on the heat treatment conditions, as well as a complete characterization of the heat-treated Ti64 bars, which were used as substrates for the thin-film coatings in the present manuscript, were provided in our previous work [44].

Briefly, the 740 °C/130 min sample retained the columnar prior β-grains extending along the build direction. Within the prior β-grains, the heat treatment promoted the α' → α + β transformation but the α-phase retained the same morphology and crystallographic orientation of the progenitor α'-martensite, with fine laths of sub-micrometre width [49]. Sub-micrometric β-phase was precipitated along the α-lath grain boundaries due to the diffusion of the β-stabilizing alloying elements (V, Fe) contained in the α'-martensite. At the solubilization temperature of 1050 °C (i.e., above the β-transus), by contrast, the columnar β-grains recrystallized into equiaxed ones, while the subsequent cooling process in argon resulted in a microstructure formed by coarser α + β colonies, arranged in a Widmanstätten structure, as well as a globular-shaped α-phase [44].

The mechanical properties of these samples, again from [44], are summarized in Table 1. Consistent with the microstructural differences recalled above, the treatment at the higher temperature resulted in slightly lower hardness and mechanical strength but slightly better elongation to fracture [44], compared to the treatment below the β-transus.

The heat-treated bars, after separation from the platform, were cut in several plates having a base and height of 12.3 × 15 mm^2 and 5 mm, respectively. Because many different surface finishing processes can be applied, which result in different surface textures, in this work we chose to study two different finishes of the Ti64 substrates, obtained by grinding with SiC papers of different grit sizes.

The roughness of the substrates was characterized by a non-contact 3D profilometer (Taylor Hobson, Leicester, United Kingdom) equipped with the Mountains® platform software through which the main roughness parameters, summarized in Table 2, were obtained. The "smooth" substrate has notably lower roughness amplitude (Sa, Sq, Sz) and a more markedly negative skewness (Ssk), since finer grinding smoothed out the roughness peaks left by coarser abrasives, but it did not remove some of the deepest dales. Smoothing also reduced the arithmetic mean peak curvature (Spc), i.e. the peaks have a larger curvature radius. For each condition, roughness parameters were evaluated on a substrate area of 9.20 mm^2, which was composed by four images of 2.30 mm^2 arranged in a 2 × 2 matrix.

2.2. Deposition of the coatings

Two types of coatings were deposited on all types of substrates: a Diamond-Like Carbon (DLC)-based coating and an AlCrN coating. Depositions were carried out at an industrial facility in order to obtain samples that are fully representative of the state of the art.

The DLC-based coating was deposited using a combined PVD + PE-CVD system (Hauzer HTC-1200) comprising 4 magnetron sputtering (MS – UBM) sources with 2 × Cr + 2 × WC targets and a pulsed bias power supply (60 kHz) for PE-CVD plasma generation.

The deposition chamber was evacuated to a base pressure of 10^{-5} mbar range and heated to 180 °C. Substrate cleaning was performed by Argon plasma etching, followed by sequential deposition of a metallic Chromium adhesion layer (2 × Cr, 5 kW, only Argon) and a subsequent support layer made by a W-C:H structure (2 × WC, 8 kW, Argon + Acetylene). The top functional layer is done by pure Acetylene plasma, using pulsed biasing to generate radicals for film formation.

The AlCrN coating was deposited using a High-Power Impulse Magnetron Sputtering (HiPIMS) system (CemeCon CC800 HiPIMS) comprising 4 HiPIMS sources each equipped with an AlCr 70/30 target.

The deposition chamber was evacuated to a base pressure in the low-10^{-5} mbar range and heated to 470 °C. Substrate cleaning was performed by MF Argon etching, followed by deposition of an AlCrN monolayer (4 × AlCr, 8 kW, Ar + N_2).

In this case, one additional sample was also deposited onto a silicon wafer to observe the fractured section of the AlCrN coating after manual breaking of the coated sample.

2.3. Samples characterization

The top surfaces and cross-sections of the coatings were observed by scanning electron microscopy (SEM: Nova NanoSEM 450, FEI – Thermo Fisher Scientific, Eindhoven, NL) equipped with an energy-dispersive X-ray (EDX) detector (Quantax-200, Bruker Nano GmbH, Berlin, Germany). Top surfaces were observed "as-is" after ultrasonic cleaning in acetone to remove any contamination. Cross-sections were prepared by cutting the coated samples with a SiC-based abrasive disc and were mounted in a two-component epoxy resin. The mounted samples were subsequently ground with SiC papers (from P400 to P2500) and sequentially polished with a polycrystalline diamond slurry (3 μm average particle diameter) and a colloidal silica suspension (50 nm average particle size). The samples were lightly etched with Keller's reagent to increase the contrast between the coating and the etched substrate, and ultrasonically cleaned in ethanol. The cross-sections were observed both without any metallization, and after sputter-coating with a thin (≈10 nm) layer of gold to improve image stability (especially for EDX line-scanning).

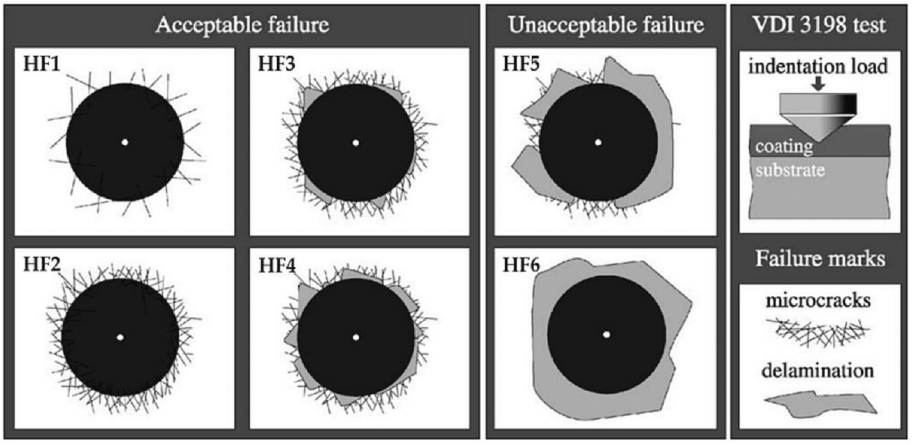

Fig. 1. Failure chart of the VDI 3198 indentation test (Reprinted from reference [51]).

Additional cross-sectional observations on the AlCrN film were performed on a fractured surface obtained by manually breaking the sample deposited onto a silicon wafer.

Micro-Raman spectra were acquired on the top surfaces of the coatings using a LabRam HR spectrometer (Horiba, Palaiseau, France). A 532 nm-wavelength laser source with 100 mW power was focused through a 100× objective (numerical aperture 0.9) and analysed with a 600 g/mm diffraction grating. Spectra on DLC-based coatings were acquired by filtering the laser power to 25 % of its maximum, operating over a 700–2100 cm^{-1} spectral range, integrating 10 acquisitions of 20 s duration each. Spectra on AlCrN coatings were acquired by filtering the laser power to 10 % of its maximum, over a 100–1700 cm^{-1} range, integrating 3 acquisitions of 80 s duration each.

Nanoindentation tests (NHT^3, Anton Paar – Tritec, Corcelles, CH) were performed on the top surfaces of DLC-based and AlCrN films deposited onto smooth substrates in both heat-treatment conditions, because the rough surface would cause excessive data scatter and too many anomalous load-penetration curves as the indenter touches non-planar portions of the surface. Tests were carried out using a Berkovich tip which is periodically calibrated and verified against a fused silica reference according to the ISO 14577-2 standard. A maximum load of 10 mN, a loading and unloading duration of 30 s, and a holding time of 15 s at maximum load were employed. A total of 100 indentations were performed on each sample. Data were analysed in accordance with the ISO 14577-1 standard, calculating the elastic modulus E_{IT}, the indentation hardness H_{IT}, and its conversion to Vickers hardness HV.

Scratch tests (Micro-Combi Tester, Anton Paar – Tritec) were performed on all film/substrate combinations using a Rockwell-type conical diamond indenter with a 100 μm-radius tip. Three tracks were performed on each surface, with a track length of 6 mm, a speed of 6 mm/min, and a load range from 0.02 N to 30 N. Critical loads were identified by optical microscopy using a 20× objective, following the classification given in the ISO 20502 standard.

Rockwell VDI tests were performed as prescribed by the VDI 3198 standard [50], using a conical diamond indenter and a load of 150 kg, to evaluate the coating-substrate system adhesion. The measurements were performed at room temperature by using ZHR Rockwell hardness testers (Zwick/Roell, Ulm, Germany). Crack formation and delamination of both the DLC-based and AlCrN coatings were first evaluated by comparing the imprints observed using an inverted-light optical microscope (OM: Leica DMi8 Leica, Wetzlar, Germany) and the failure chart in Fig. 1. Secondly, the number of cracks formed along the imprint border and the percentage of the detached area were evaluated and then correlated to each other. In the former case, the number of cracks was calculated per unit length [mm], since the diameter of the Rockwell indentation varies in relation to the substrate hardness. In the second case, the percentage of detached areas was evaluated considering a circular crown, having a width that was evaluated as 5 % of the radius of the Rockwell indentations. Obviously, all circular crowns contained all detached areas observed through the OM investigations.

Table 3
Surface roughness parameters of the Al_2O_3 counterpart.

Parameter [unit]	Value
Sa [μm]	0.023 ± 0.002
Sq [μm]	0.040 ± 0.005
Sz [μm]	1.63 ± 0.35
Ssk	−1.65 ± 3.45
Spc [mm^{-1}]	34.5 ± 3.9

Rockwell imprints were also investigated through focused ion beam scanning electron microscopy (FIB-SEM: Auriga Compact FIB-SEM, Zeiss, Oberkochen, Germany) equipped with the Ultim® Extreme detector (Oxford Instruments, Abingdon, United Kingdom). Each sample was tilted at 54° such that the imprint was perpendicular to the FIB, and areas along the indentation boundary were milled using 20 keV Ga^+ ions with a current of 5 nA and a milling depth of 10 μm. SEM images of FIB cross-sections were acquired keeping constant the tilt angle (36°).

2.4. Sliding wear testing

Unidirectional ball-on-disc sliding wear tests (THT, Anton Paar – Tritec) were performed at room temperature using a 3 mm-diameter sintered Al_2O_3 ball (Anton-Paar) as counterpart. The roughness of the counterpart was check by a structured illumination microscope (ConfoCam, Confovis GmbH, Jena, Germany) by acquiring the surface profile

Table 4
Average (p_{avg}) and maximum (p_{max}) hertzian contact pressures, maximum sub-surface shear stress (τ_{max}) and depth of the sub-surface shear stress maximum (Depth) at the beginning of the ball-on-disc tests.

	p_{avg} [GPa]		p_{max} [GPa]		τ_{max}* [GPa]		Depth* [μm]	
	Load [N]							
Sample	5	10	5	10	5	10	5	10
DLC (740 °C-HT substrate)	1.4	1.7	2.1	2.6	0.64	0.81	16	21
DLC (1050 °C-HT substrate)	1.3	1.6	1.9	2.4	0.59	0.74	17	21
AlCrN (740 °C-HT substrate)	1.8	/	2.7	/	0.83	/	14	/
AlCrN (1050 °C-HT substrate)	1.8	/	2.7	/	0.82	/	14	/

* Values computed for a Poisson's ratio of 0.30.

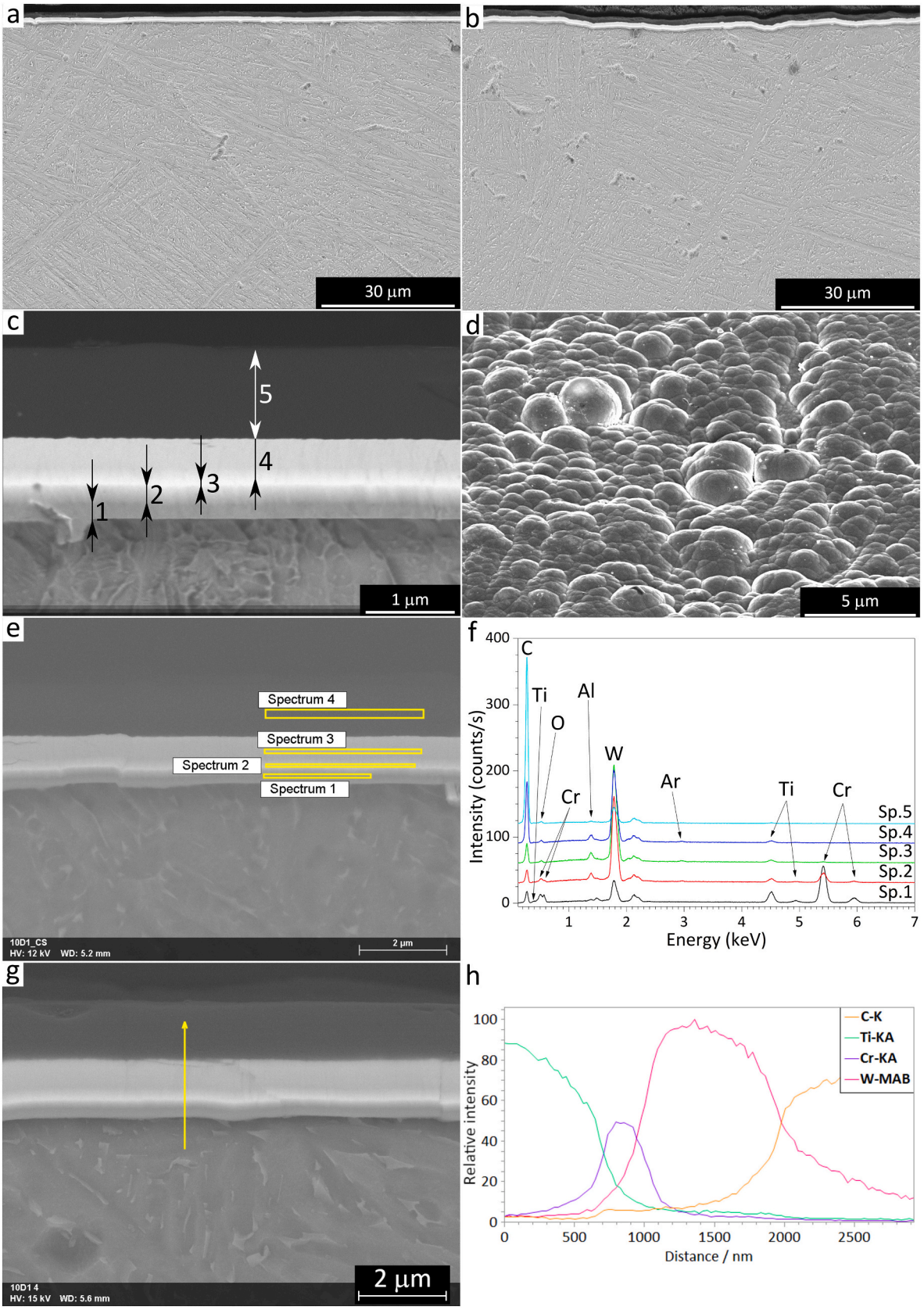

Fig. 2. SEM micrographs of DLC-based films deposited onto substrates heat-treated at 1050 °C: general cross-sectional views on smooth (a) and rough (b) substrate, magnified detail on smooth substrate (c) and top-surface detail (d); backscattered electrons view (e) with corresponding EDX spectra (f), and another backscattered electrons view (g) with EDX linescan (h). Labels 1–5 in panel (c) indicate the identifiable layers – see the text for a description.

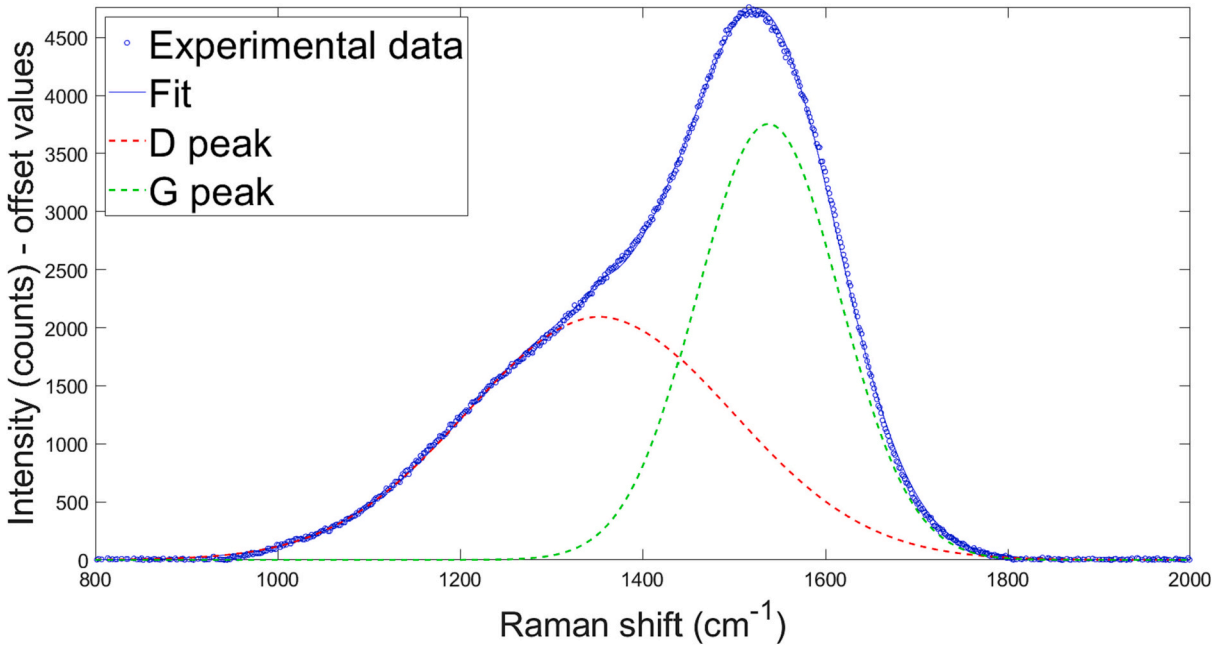

Fig. 3. Example of a (background-subtracted) micro-Raman spectrum acquired on the DLC-based film deposited onto a smooth Ti64 substrate heat-treated at 1050 °C, outside the ball-on-disc wear track, with peak fitting.

of three balls at two random locations each, operating with a 20× objective over a ≈ 0.5 × 0.5 mm^2 area with a z-step size of 0.1 μm. The profiles were processed according to the workflows given in ISO 25178-2 and the results are summarized in Table 3.

The ball-on-disc setup with an Al_2O_3 counterpart was chosen because, in the authors' experience, it is suitable to provide a simplified simulation of the contact conditions encountered in several applications that involve sliding against counterparts containing hard phases (e.g. rotary seals, journal bearings, etc.). Tests on all DLC-coated samples were performed at both 5 N and 10 N normal load to check for the effect of the nominal (initial) contact pressure, with a sliding distance of 1000 m, a sliding speed of 0.20 m/s and a wear track radius of 4 mm. Following some preliminary experiments, tests on AlCrN samples were performed only at 5 N load with a sliding distance of 250 m, and only with "smooth" substrates (see the discussion in Section 3.3.1 for details on the reasons for this choice).

Table 4 shows estimates of the nominal contact pressures and sub-surface shear stress maxima acting on the samples at the beginning of the sliding wear test (before mutual wear caused the ball and the coated samples to conform to each other) under the normal loads mentioned above. The values were computed using Hertz's formulae for a sphere-on-flat contact, using the elastic moduli of the coatings as listed in Section 3.1 and assuming that the elastic modulus of the Al_2O_3 ball was 370 GPa [52] and that Poisson's ratios were 0.22 for both Al_2O_3 [52] and the two coatings [53]. It is important to remark that the values in Table 4 are purely indicative, mostly because Hertz's equations are valid only for homogeneous materials, whilst the present samples are coated. Accordingly, the computed depth of the sub-surface shear stress maximum shows that it falls below the coating (Table 4). Hence, it would be necessary to account for the mechanical properties of both the coating and the substrate, which would likely yield lower values for the nominal (average and maximum) contact pressures and shear stresses and higher sub-surface depths of the shear stress maximum. The elastic modulus of the Ti-6Al-4V substrate is indeed lower than that of the coatings and introduces more compliance into the system.

The friction coefficient was calculated during the ball-on-disc test by measuring the tangential force acting on the ball-holding arm with a load cell. The wear volume loss of the ball was calculated by measuring the diameter of the circular wear scar with an optical microscope (Olympus GX51). The volume loss of the coating was measured by acquiring the profile of the wear track with a structured illumination microscope (ConfoCam) operating with a 50× objective (0.80 numerical aperture) and a 0.05 μm z-scan step size. Four 340 × 340 μm areas were acquired along the wear scar: from the wear scar volume within each area, an average cross-sectional wear scar area was computed and subsequently multiplied by the length of the circular track to obtain the overall volume.

Micro-Raman spectra were acquired on worn coating surfaces and on any wear debris found around the wear track, using the same conditions listed in Section 2.3. To acquire spectra on the debris of the DLC-based coatings, the laser power was filtered to 10 % instead of 25 % to prevent any thermal alteration.

The worn surfaces of the samples were observed first by optical microscopy (Olympus GX51) and then, after ultrasonic cleaning in acetone to remove any loose debris, by SEM (Nova NanoSEM 450). Cross-sections of selected samples were prepared according to the same cutting, mounting, grinding, polishing and etching procedures listed in Section 2.3.

3. Results and discussion

3.1. *Structure, microstructure and micromechanical properties of the films*

On both smooth (Fig. 2a) and rough (Fig. 2b) surfaces, the DLC-based films follow the substrate profile. As was expected, the deposition of these films did not cause any visible microstructural alteration in the near-surface region of the substrate. Indeed, the deposition occurred at temperatures far below the heat treatment temperatures of the substrates and ionic bombardment during deposition was not strong enough to produce significant effects.

In more detail, the SEM analysis (Fig. 2c) together with related EDX spectra (Fig. 2e, f) and EDX linescans (Fig. 2g, h) highlight the multi-layered architecture of the DLC-based film. A Cr-based interlayer (Fig. 2c – label 1, EDX spectrum 1 in Fig. 2e, f), a Cr—W layer (Fig. 2c – label 2), a WC-based layer (Fig. 2c – label 3, EDX spectrum 2 in Fig. 2e, f), and a WC-C layer with slightly higher C/W ratio (Fig. 2c, label 4, EDX spectrum 3 in Fig. 2e, f) constitute the adhesion layers that provide a

Table 5
Nano-indentation results for coatings onto smooth substrates.

	E_{IT} [GPa]	H_{IT} [GPa]	HV
DLC (740 °C-HT substrate)	218 ± 74	27.2 ± 9.5	2517 ± 882
DLC (1050 °C-HT substrate)	179 ± 15	22.4 ± 2.8	2076 ± 259
AlCrN (740 °C-HT substrate)	444 ± 160	33.6 ± 12.6	3113 ± 1164
AlCrN (1050 °C-HT substrate)	430 ± 199	33.3 ± 13.3	3087 ± 1232

smooth transition from the substrate to the DLC top layer in terms of both chemical composition and mechanical properties. The overall thickness of the film is 2.1 ± 0.1 μm, with an approximately 1:1 thickness ratio between the interlayer system and the top layer (the DLC layer being 1.1 ± 0.1 μm thick, Fig. 2c, label 5). In a magnified view, the top surface of the DLC film is characterized by a cluster morphology (Fig. 2d) that is typical of this type of coating [54].

The DLC film does not contain any detectable doping elements: EDX signal from W and minor peaks from Al and Ti (Fig. 2e, f – spectrum 5 and linescans in Fig. 2g, h) are due to some contribution from the substrate and the underlying layers because of the spread of the electron interaction volume in the sample at 15 kV acceleration voltage.

A representative micro-Raman spectrum of the DLC top layer, which is unaffected by the substrate characteristics, is shown in Fig. 3, and it is typical of hydrogenated amorphous carbon (a-C:H) layers obtained by a PE-CVD process [55–57]. Fitting of the "D" and "G" bands with pseudo-Voigt functions (Fig. 3) allows to identify characteristic parameters, specifically the G-peak position at approximately 1535 cm^{-1} and the intensity ratios between the D and G bands (I(D)/(G)) of around 0.6. Based on the trends published by Ferrari and Robertson [55], both values consistently indicate a fraction of sp^3 C—C bonds of about 40 at. %. The absence of a photoluminescence background (i.e. a linearly increasing background intensity in the Raman spectra) indicates that the hydrogen content in the film is below the limit at which such background starts appearing. Marchon et al. identified this limit at about 34 at.% [58]; the more extensive dataset by Casiraghi et al. further clarified that, with a negligible background slope, the H content is not greater than 20 at.% [57], even though it should be remarked that both of the studies mentioned above employed a laser excitation wavelength of 514 nm, slightly different from the 532 nm source employed in this work (Section 2.3).

Nanoindentation tests (Table 5) returned hardness values in the range of 2100–2500 HV and elastic moduli around 200 GPa for the DLC

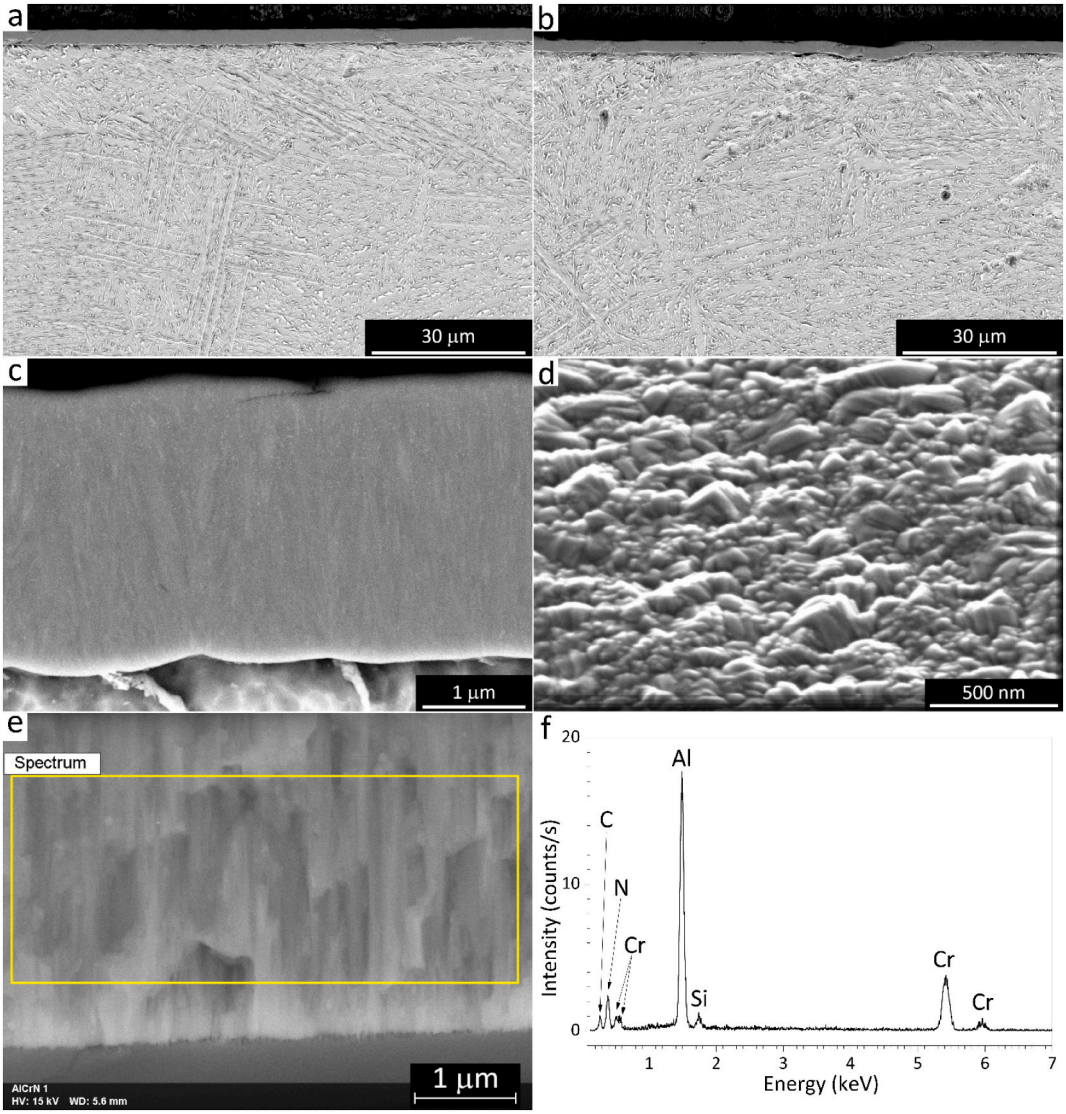

Fig. 4. SEM micrographs of AlCrN films deposited onto substrates heat-treated at 740 °C: general cross-sectional views on smooth (a) and rough (b) substrate, magnified detail on smooth substrate (c) and top-surface detail (d); fractured section of the AlCrN film deposited onto a silicon wafer (e) with corresponding EDX spectrum (f).

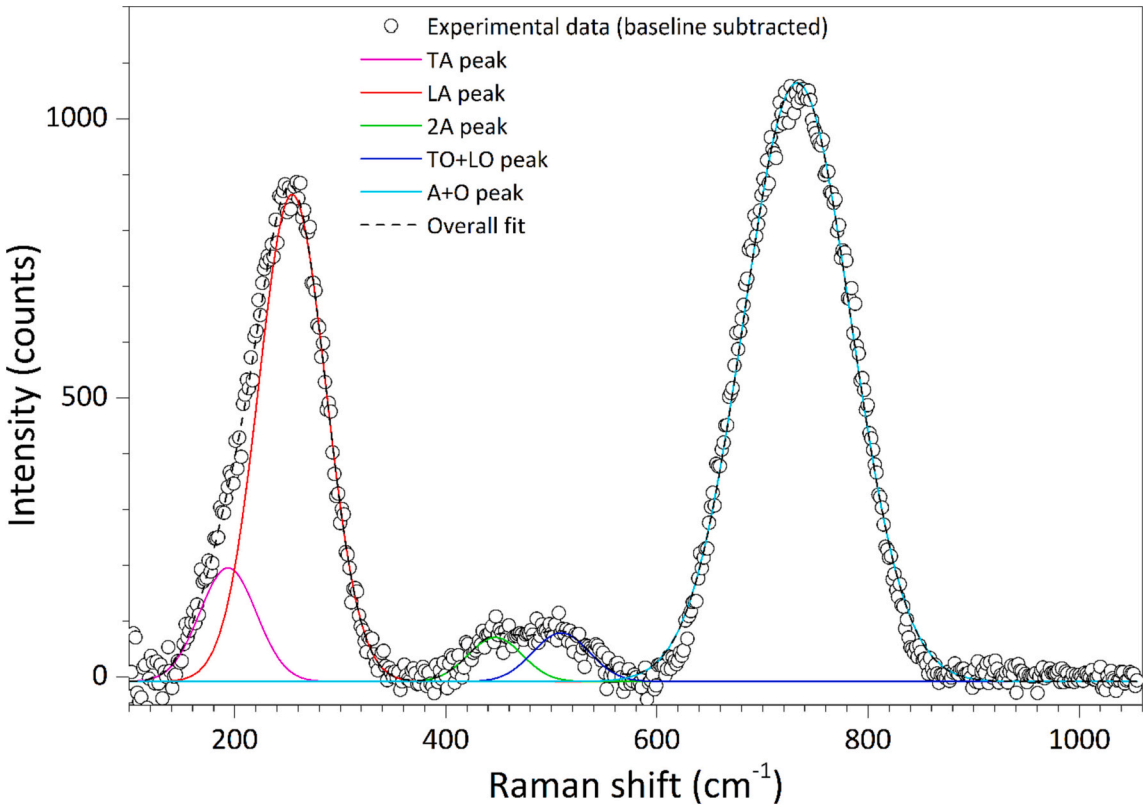

Fig. 5. Example of a (background-subtracted) micro-Raman spectrum acquired on the AlCrN film deposited onto a smooth substrate heat-treated at 1050 °C outside the wear track, with peak fitting.

layer. The data exhibited somewhat large error ranges, because even the smooth substrates still exhibited a non-negligible roughness (Table 2), whose amplitude was slightly increased by the topographical features of the film itself (Fig. 2d). Roughness is known to increase the scatter of depth-sensing indentation results [59]. Nonetheless, these values fall squarely within the typical range for a-C:H films [22].

It is further noted that the maximum penetration depth in the present nanoindentation experiments was around 180–190 nm, i.e. <10 % of the overall film thickness and a bit less than 20 % of the thickness of the DLC top layer. Thus, the present results are mainly sensitive to the properties of the top layer itself.

Casiraghi et al. [57] suggested that the mechanical properties of an a-C:H film correlate with the width of the G-band in its Raman spectrum. In fact, the latter parameter reflects the amount of C—C sp^3 bonds, which contribute the most to the creation of the three-dimensional glassy network of the film and, therefore, are mostly responsible for its strength and stiffness. Trends of elastic modulus as a function of the full width at half-maximum height (FWHM) of the G-band (albeit for a 514 nm-wavelength excitation source, as noted previously) [57] show that, with a FWHM around 195 cm^{-1}, as in our case (Fig. 3), the elastic modulus should be around 200 GPa. This result is in particularly good agreement with the nanoindentation data in Table 5, thus confirming that the present films have the typical properties of a-C:H.

The AlCrN coating also follows the profile of both the "smooth" and "rough" substrates (Fig. 4a and b, respectively) with no microstructural alteration in the near-surface region of the substrate. It consists of a 2.9 ± 0.2 μm thick layer made of densely packed, slightly tapered columnar grains identifiable both by the electron channelling contrast in the backscattered electrons – SEM view of Fig. 4c and in the fracture surface of the coating deposited onto a silicon wafer in Fig. 4e. The angular extremities of those fine columnar grains are also visible in a magnified view of the top surface (Fig. 4d). This dense microstructure is typical of "zone T" according to the modified Thornton model of possible PVD films' microstructures [60].

The AlCrN film is compositionally uniform. Quantitative analysis based on EDX spectra acquired on the fractured section of the AlCrN film (such as the spectrum shown in Fig. 4f) indicates an Al fraction of 0.61 ± 0.01. According to Kaindl et al. [61,62], it is also possible to derive compositional information on AlCrN films from their Raman spectra (Fig. 5). Indeed, although the centrosymmetric structure of AlCrN, which possesses the same face-centred cubic lattice of pure AlN and CrN up to an Al fraction of 0.7, should not exhibit any Raman scattering, the distortions and defects brought about by the mixing of Al and Cr in the lattice sites cause symmetry violations and result in Raman scatting from the defect sites themselves [62]. Specifically, the position of the Raman scattering band due to combined acoustic and optic vibration modes (A + O), ν_{A+O}, located roughly in the 700–750 cm^{-1} region, is correlated to the Al fraction, χ_{Al}, by the relation $\chi_{Al} \approx (\nu_{A+O} - 629.58)/174.84$ [62]. Fitting of our Raman spectra (Fig. 5) shows that the A + O band of the present AlCrN samples is centred in the range from 722 to 732 cm^{-1}. According to the above relation, this corresponds to $\chi_{Al} \approx 0.53–0.58$, which is in fairly good agreement with the EDX results, considering the approximate nature of the extrapolation from Raman spectra (on the one hand) and the limits to the quantitative accuracy of the EDX method (on the other hand).

In terms of micromechanical properties, the AlCrN film, irrespective of the heat treatment condition of the substrate, is characterized by higher hardness and much higher elastic modulus than the DLC-based one (Table 5), which also means that the AlCrN film has lower H/E ratio than the DLC-based layer. Hardness values around 33–34 GPa are quite consistent with the values of 32.5 ± 6.5 GPa [63] and 31.6 ± 1.0 GPa [48] listed in the literature for AlCrN films with Al fractions of 70 % and 60 %, respectively.

Table 6
Critical loads measured by scratch testing and VDI class for all coating/substrate combinations.

Sample	L_{C2} [N]	L_{C3} [N]	Delamination [N]	VDI class
DLC (740 °C-HT substrate – smooth)	7.7 ± 1.0	13.1 ± 4.1	15.0 ± 2.5	HF3
DLC (740 °C-HT substrate – rough)	6.7 ± 3.7	11.2 ± 3.5	14.0 ± 3.9	
DLC (1050 °C-HT substrate – smooth)	5.5 ± 4.7	6.0 ± 4.2	12.8 ± 1.7	
DLC (1050 °C-HT substrate – rough)	4.9 ± 0.8	8.5 ± 0.6	11.1 ± 0.7	
AlCrN (740 °C-HT substrate – smooth)	10.2 ± 0.9	15.0 ± 4.9	19.5 ± 1.6	HF3
AlCrN (740 °C-HT substrate – rough)	10.1 ± 0.7	11.2 ± 1.7	17.3 ± 0.6	
AlCrN (1050 °C-HT substrate – smooth)	1.0 ± 0.3	5.7 ± 0.9	12.8 ± 0.5	HF2
AlCrN (1050 °C-HT substrate – rough)	7.1 ± 2.3	7.1 ± 2.3*	16.6 ± 0.5	

* In this sample, L_{C2} and L_{C3} were always coincident, i.e. the first chipping directly extended across the entire width of the scratch track.

3.2. Adhesion/cohesion strength

Scratch tests allow the identification of the L_{C2} and L_{C3} critical loads as defined in the ISO 20502 standard, namely the load for the onset of chipping damage and the load for the first continuous chipping across the track width. Additionally, the delamination load, i.e. the load for continuous perforation of the film, is also identifiable. On the other hand, it was not possible to identify with confidence the L_{C1} critical load for the onset of cracking, because the surface irregularities, even on the smooth substrate, are such that the earliest, smallest cracks are hardly visible.

With both DLC-based and AlCrN films, the results (Table 6) show few differences in scratch performance between smooth and rough substrates. On the other hand, despite the scatter in some of the data, a difference emerges between the scratch adhesion/cohesion of films deposited on the harder substrate, heat-treated at 740 °C, and on the softer one, heat-treated at 1050 °C. As could be expected, indeed, the softer substrate systematically results in lower critical loads. As explained in the Introduction, due to their higher hardness the films cannot follow the extensive plastic deformation that the substrate undergoes once it yields. Therefore, as the softer substrate starts to deform plastically at lower loads during the scratch test, it causes the coatings to experience overloading and cracking earlier than does the harder substrate. This mechanism was confirmed by Wang et al. [15] through finite element modelling of scratch tests on thin films deposited onto grade-2 titanium substrates in the as-supplied condition or after mechanical hardening.

The scratch failure modes seen in both DLC-based and AlCrN films were quite similar (Fig. 6). First, at the critical load L_{C2}, the outer part of the coating chipped off the side of the scratch track (see the magnified details taken at loads above L_{C2} in Fig. 6). The spalled areas became progressively larger with further increases in load, until they extended across the entire width of the track at L_{C3} (Fig. 6). Then, at the delamination load, the entire coating was spalled off and the substrate was exposed.

In more detail, the initial chipping failure at L_{C2} and L_{C3} never occurred at the coating/substrate interface. In the DLC-based film, the rounded cracks typical of an amorphous material propagated across the

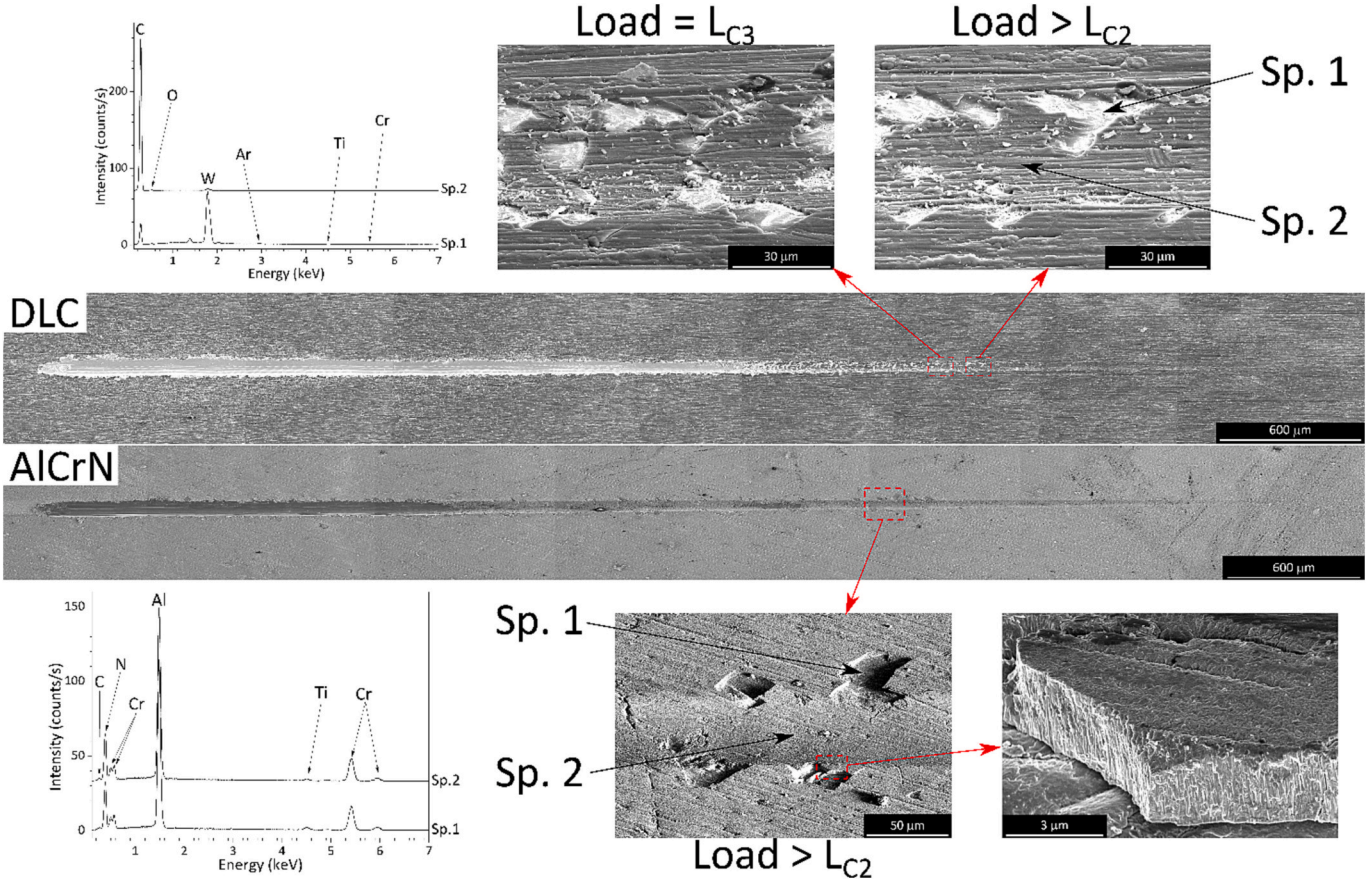

Fig. 6. SEM overviews of scratch tracks onto the DLC-based (a) and the AlCrN (b) film, both deposited onto the smooth substrate heat-treated at 740 °C, with magnified details and EDX spectra. The overview images were obtained by stitching of multiple secondary electron-SEM micrographs.

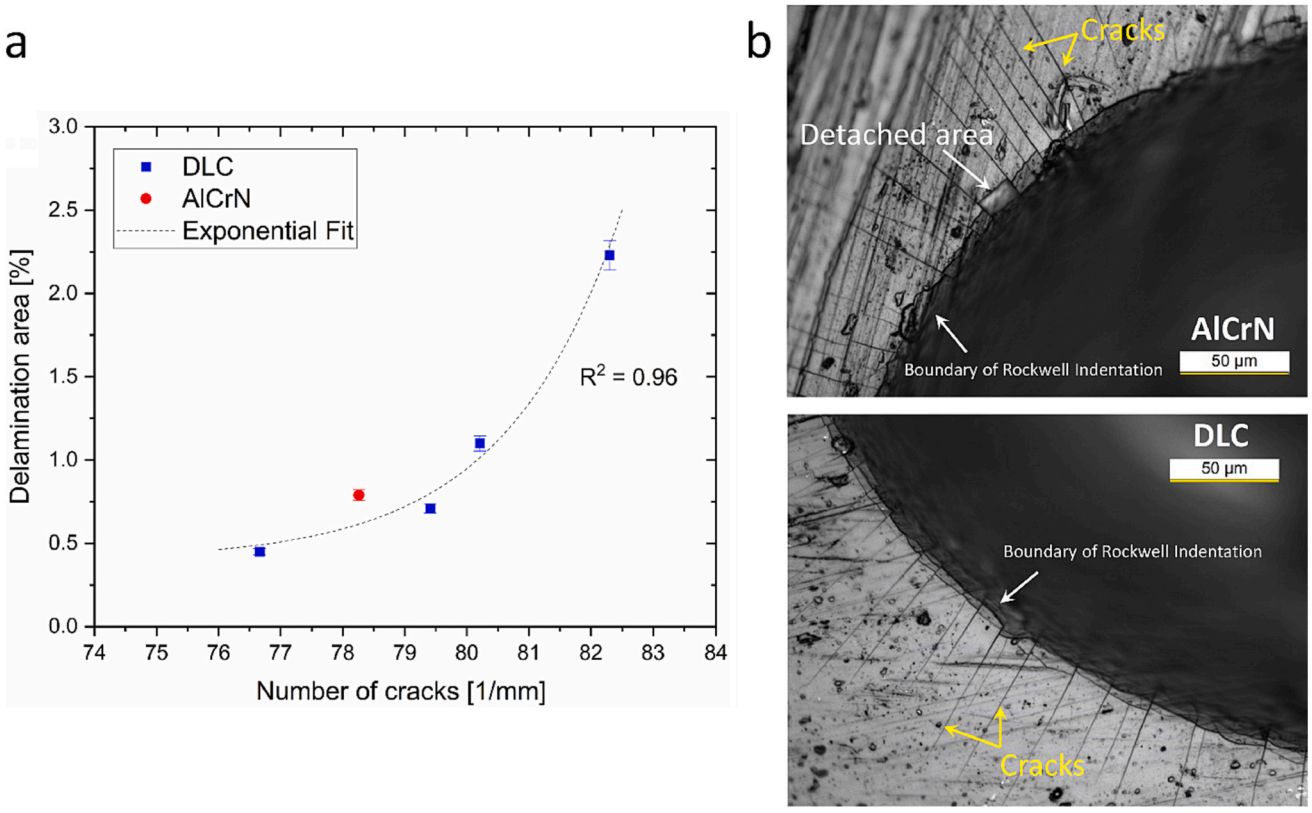

Fig. 7. Correlation between the percentage of delaminated area and number of cracks per mm (a) in all samples that exhibited an HF3 response. The optical microscope micrographs show a portion of the Rockwell indentation performed on the AlCrN and DLC (740 °C-HT substrate – smooth) films (b).

top layer and were deflected along its interface with the WC-C interlayer and/or within such interlayer, which was consequently exposed. This is seen not only by its obviously brighter contrast, but also through the EDX spectrum 1 in the magnified view of the DLC film in Fig. 6. This spectrum is dominated by an intense W peak, different from spectrum 2, acquired in an undamaged part of the track, which reveals only a minor W signal because the X-ray generation volume extends a bit deeper than the thickness of the DLC layer itself.

This suggests that the architecture of the DLC-based film provided crack deflection mechanisms that improved the interface toughness and resulted in good adhesion. In comparison, DLC-based films with simpler architectures, e.g. consisting of a single adhesion layer of CrN between the DLC layer and a β-Ti alloy (with similar mechanical properties as the present 740 °C-heat treated substrate) [64], or of a SiC adhesion layer onto a Ti-6Al-4V ELI substrate [65], exhibited L_{C2} values around 5 N when scratch-tested with a 200 μm-radius tip. This means that the simpler coating systems possessed much lower adhesion strength compared with the present samples, where higher L_{C2} values were obtained with a sharper tip. Similarly, Zhang et al. [66] found very low critical load values for DLC films deposited directly (without interlayers) onto Ti-6Al-4V by filtered cathodic vacuum arc. Wang et al. [15] and Avelar-Batista et al. [67] studied somewhat more complex architectures that provided better adhesion, yet they both reported that several types of DLC-based films deposited onto Ti-6Al-4V substrates exhibited delamination loads <30 N when tested with a standard, 200 μm-radius tip. In preliminary tests, we found that it was not possible to delaminate the present DLC-based films using a 200 μm-radius tip up to the maximum load value of 30 N afforded by the experimental apparatus, which was the reason we employed a non-standard, 100 μm-radius tip.

Similarly, in the AlCrN film, cracks proceeded transversely along the columnar grain boundaries, crossing part of the coating thickness, but they were deflected along a longitudinal path above the substrate interface (see the corresponding magnifications in Fig. 6), as confirmed by the EDX spectrum 1 in Fig. 6, where the Ti signal from the substrate becomes only marginally stronger than in the undamaged region (spectrum 2). Thus, like the DLC-based film, the AlCrN layer also possessed rather good adhesion to the substrate, so that initial failure is of a cohesive nature, and complete coating removal occurs only at a later stage.

It is concluded that, using the L-PBF Ti64 substrates (especially when subjected to the lower-temperature heat-treatment at 740 °C), we could attain an adhesion strength comparable to or significantly competitive with the adhesion to conventionally manufactured substrates.

Unlike the scratch tests, the Rockwell VDI test (Table 6) could not differentiate between the various substrate treatment conditions. The response of the DLC-based films was always attributable to the HF3 class (Fig. 7), in which both cracks and detached areas were observed by optical microscopy. This result is in line with the findings by Kashyap et al. [68], who concluded that a DLC-based coating deposited on a cast Ti6Al4V substrate through the PVD technique shows good coating/substrate adhesion (HF1-HF3). The AlCrN films exhibited only cracks but no delaminations, except for the sample with the smooth 740 °C-HT substrate, where slight delaminations also appeared. Lastly, the different substrate-coating combinations did not influence the inter-crack spacing in the AlCrN films, which remained constant at around 14 μm in all cases.

Notably, Tillmann et al. [24] found an HF4 adhesion class in the VDI adhesion test of a magnetron-sputtered, non-hydrogenated a-C film deposited on an additively manufactured α + β Ti6Al7Nb alloy similar to the present Ti64 one, which was poorer than the present results (Table 6, Fig. 7).

Despite the several coating/substrate combinations that were analysed, the fraction of delaminated area and the number of cracks were well correlated (Fig. 7a). In fact, the detached areas (white arrow in Fig. 7b) were always localized between two adjacent cracks and close to the boundary of the indentation mark; therefore, their extension

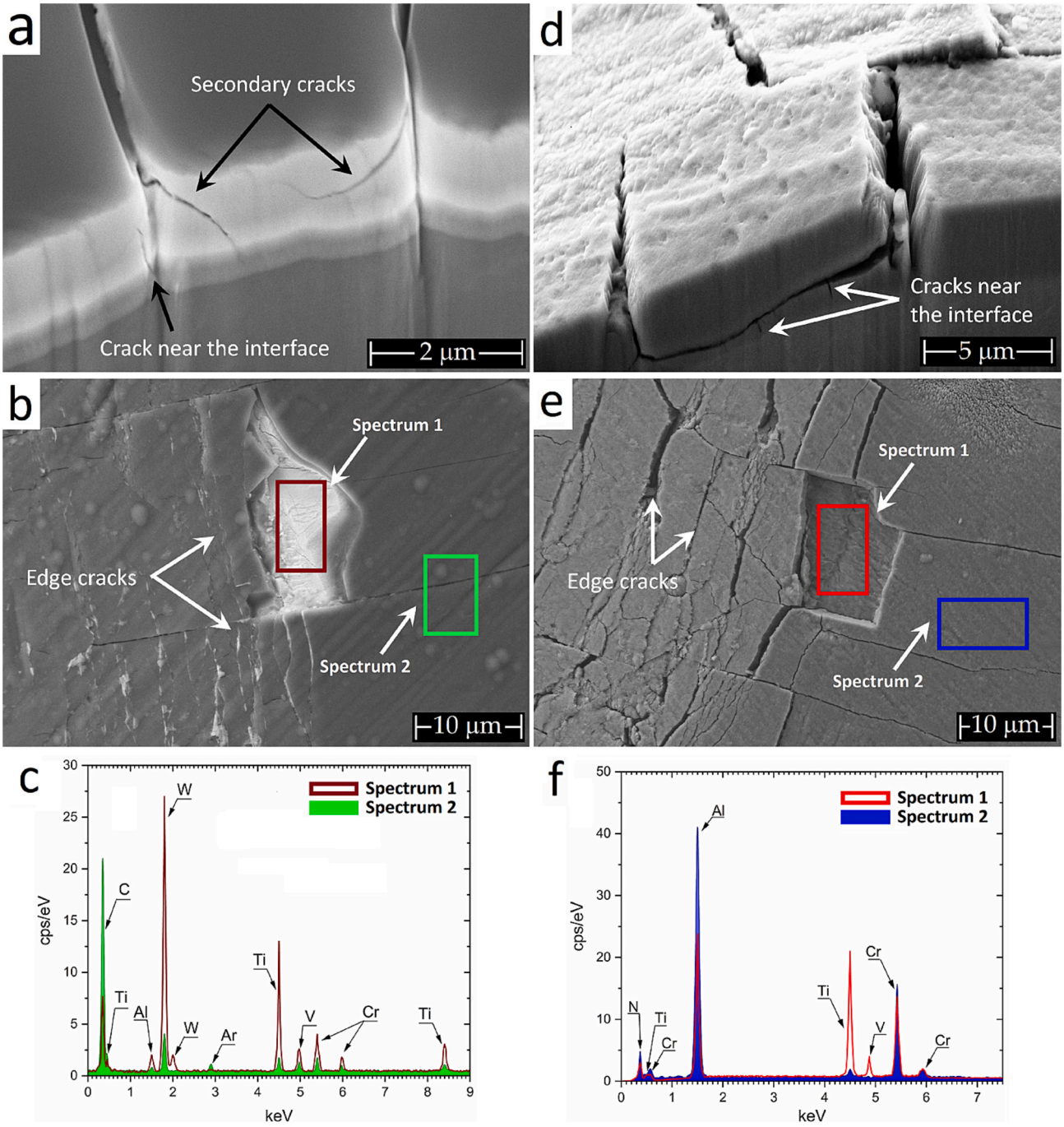

Fig. 8. SEM micrographs showing FIB cross-sections (a, d) and top surfaces (b, e) of the VDI failures of DLC-based (a, b) and AlCrN (d, e) films, and corresponding EDX spectra (c, f) that highlight the differences between the coatings and their delaminated parts. SEM images (a, b, d, e) were tilted by 36° with respect to the electron beam axis.

increased exponentially with the number of cracks (yellow arrow in Fig. 7b).

Interestingly, the same failure modes observed in the scratch test were also triggered by the VDI test, which means that both tests elicited similar damage mechanisms, although the VDI test was less sensitive to differences in adhesion/cohesion strength. More specifically, FIB cross-sections of the VDI failures (Fig. 8a) allow to confirm that cracks in the DLC-based film propagate across the WC-C interlayer rather than along its interface with the DLC top layer (Fig. 8a). This indicates a good chemical bonding between the two layers, as well as a higher toughness for the more "metallic" Cr-based underlayer. Likewise, cracks in the AlCrN film deflected in the longitudinal direction shortly above the substrate (Fig. 8b), which testifies to its good interface toughness.

As a matter of fact, the base of the delaminated areas present in both DLC-based (Fig. 8b) and AlCrN (Fig. 8e) films after the VDI tests continue to show a thin layer well-adherent to the substrate, just like in the scratch tests at loads below the delamination threshold. EDX spectra confirm the presence of W, Cr (spectrum 1 in Fig. 8b, c) and N, Al and Cr (spectrum 1 in Fig. 8e, f) in the delaminated areas of the DLC-based and AlCrN films, respectively. For these reasons, it is possible to conclude that the HF3 VDI class assigned to these samples (Table 6) should probably be considered as HF2, since the VDI 3198 standard reports that delamination must expose the substrate, although this distinction was not possible by optical microscopy inspection as prescribed by the

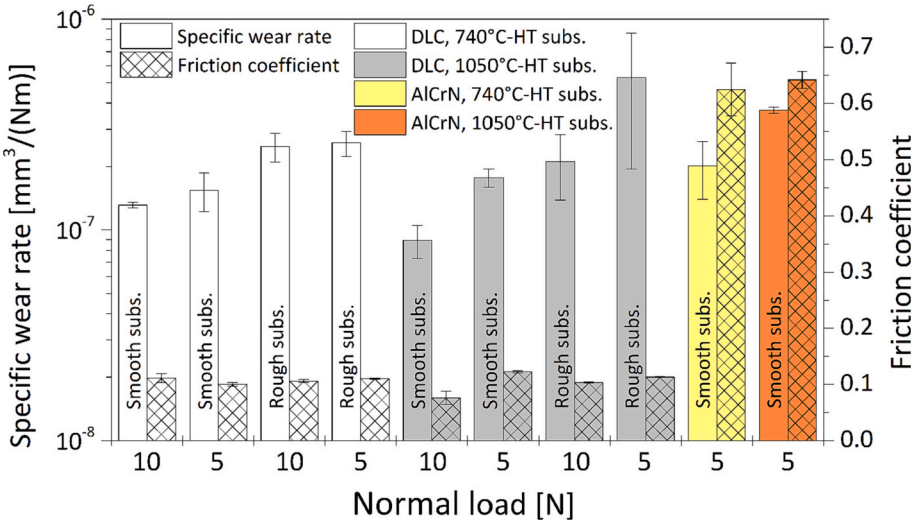

Fig. 9. Specific wear rates of the coated samples and average steady-state friction coefficients obtained through ball-on-disc testing.

standard itself.

3.3. Sliding wear behaviour

3.3.1. Specific wear rates and friction coefficients

The specific wear rates measured on the DLC-coated samples (Fig. 9) are mostly comprised between $\approx 0.9 \times 10^{-7}$ mm^3/(N•m) and $\approx 3 \times 10^{-7}$ mm^3/(N•m). These values are within the general range for a-C:H films sliding in humid air, which is reportedly 0.1–10 $\times$ 10^{-7} mm^3/(N•m) [69]. In more detail, Avelar-Batista et al. [67] reported specific wear rates of $\approx 1 \times 10^{-7}$ mm^3/(N•m) after ball-on-disc testing of several types of DLC-based films deposited onto conventionally manufactured Ti-6Al-4V substrates. It should be noted that the test conditions employed in [67] were not the same as in the present work, since a 10 mm-diameter 100Cr6 ball was employed as counterface, instead of a 3 mm-diameter Al_2O_3 ball. Nonetheless, Scharf and Singer [70] reported that the performance of DLC-based films tested against steel or alumina balls is usually similar, because the tribological behaviour is in both cases dominated by the same tribochemical phenomena based on the formation of transfer layers. Thus, it can be concluded that, also from a tribological point of view, the present DLC-based films deposited on L-PBF Ti64 substrates have analogous performance as those deposited onto conventionally manufactured substrates.

A detailed comparison between the sliding wear rates of the various DLC-coated samples (Fig. 9) shows that, contrary to the scratch adhesion results, the heat treatment of the substrate had little effect on the tribological performance of the system, whilst the roughness of the substrate did have a significant effect. Specific wear rates are also very slightly higher at the lower load of 5 N (i.e. the overall wear volume increases slightly less than linearly with the applied load), but the differences are of the same order as the associated error ranges and are therefore of little significance. Average steady-state friction coefficients, on the other hand, are always around 0.1 irrespective of the substrate condition and the applied normal load (Fig. 9). The friction curves are indeed very similar to one another (Fig. 10a-d) and show that the steady state was usually attained within <50 m of sliding, though a few curves exhibit a slightly unstable trend and/or some oscillations.

The tribological response of the AlCrN film was conspicuously different. First, it produced much higher average friction ($\mu \approx 0.65$ at the steady state, Figs. 9 and 10e). Notably, Chen et al. [48] also found identical friction coefficient values of ~0.66 in a dry sliding ball-on-disc wear test of AlCrN films against Al_2O_3 in air. Other authors reported friction coefficient values roughly comprised between 0.6 and 0.8 for unidirectional ball-on-disc tests of AlCrN coatings against Si_3N_4 balls [63,71–73]. Second, the AlCrN films could not withstand the same sliding distance of 1000 m that was used to test the DLC-based films. The friction curve in Fig. 10f shows that the AlCrN film deposited on "smooth" substrates delaminated after approximately 450 m of sliding, when the friction coefficient value first became unstable and, then, dropped to a lower level with significantly greater instability as the hard Al_2O_3 ball (and the trapped debris) cut through the uncovered titanium substrate. On rough substrates, delamination happened almost instantly at the beginning of the test, i.e. after sliding for just a few metres, so that no results could be provided in Fig. 9.

For these reasons, systematic wear tests were only performed with smooth substrates and at 5 N load, over a distance of 250 m (see Section 2.4). Within the 250 m distance, the specific wear rate of the AlCrN films was comparable to that of the DLC-based ones (Fig. 9), which means that the films were in a mild wear regime. Other authors also found specific wear rates in the mild wear range of 10^{-7} to 10^{-6} mm^3/(N•m) in unidirectional dry sliding tests of AlCrN films against various counterbodies, even when the films were deposited onto very hard substrates capable of providing better mechanical support, like cemented carbides [71,73,74]. Only in one case was a lower specific wear rate of $\sim 5 \times 10^{-8}$ mm^3/(N•m) found for an AlCrN film onto a cemented carbide substrate after dry sliding against an Al_2O_3 ball [48].

3.3.2. Wear mechanisms: DLC-based films

Analysing the wear mechanisms, DLC-based coatings onto smooth surfaces tested at 5 N load (Fig. 11a, b) show mild abrasive (polishing) wear together with the tribochemical effects typical of DLC-based films. Namely, some debris was found around the wear scars after the sample (Fig. 11a – circled area) and the counterbody (Fig. 11b - arrows) were removed from the tribometer at the end of the test.

Raman spectra acquired on the debris around the wear scar on the coated sample (Fig. 12b) differ from those found on the as-deposited films: the more pronounced D-band is typical of disordered graphite, i.e. debris graphitization occurred [22,69]. The graphitization process was limited to the debris: the Raman spectra acquired on the coating itself inside the wear scars (Fig. 12a) are qualitatively identical to those acquired on the pristine (unworn) surface, i.e. there was no tribochemical alteration of the DLC film. Fitting of the Raman spectra confirms that G-band positions, I(D)/I(G) intensity ratios, and the FWHM of the G band obtained inside the wear scars are identical (within error range) to those found outside the wear scars on the same samples (Table 7). Thus, it is inferred that the stably low friction coefficient seen in Figs. 9 and 10a-d resulted from the presence of graphitized debris. Although the debris was seen along the edges of the wear scars when the

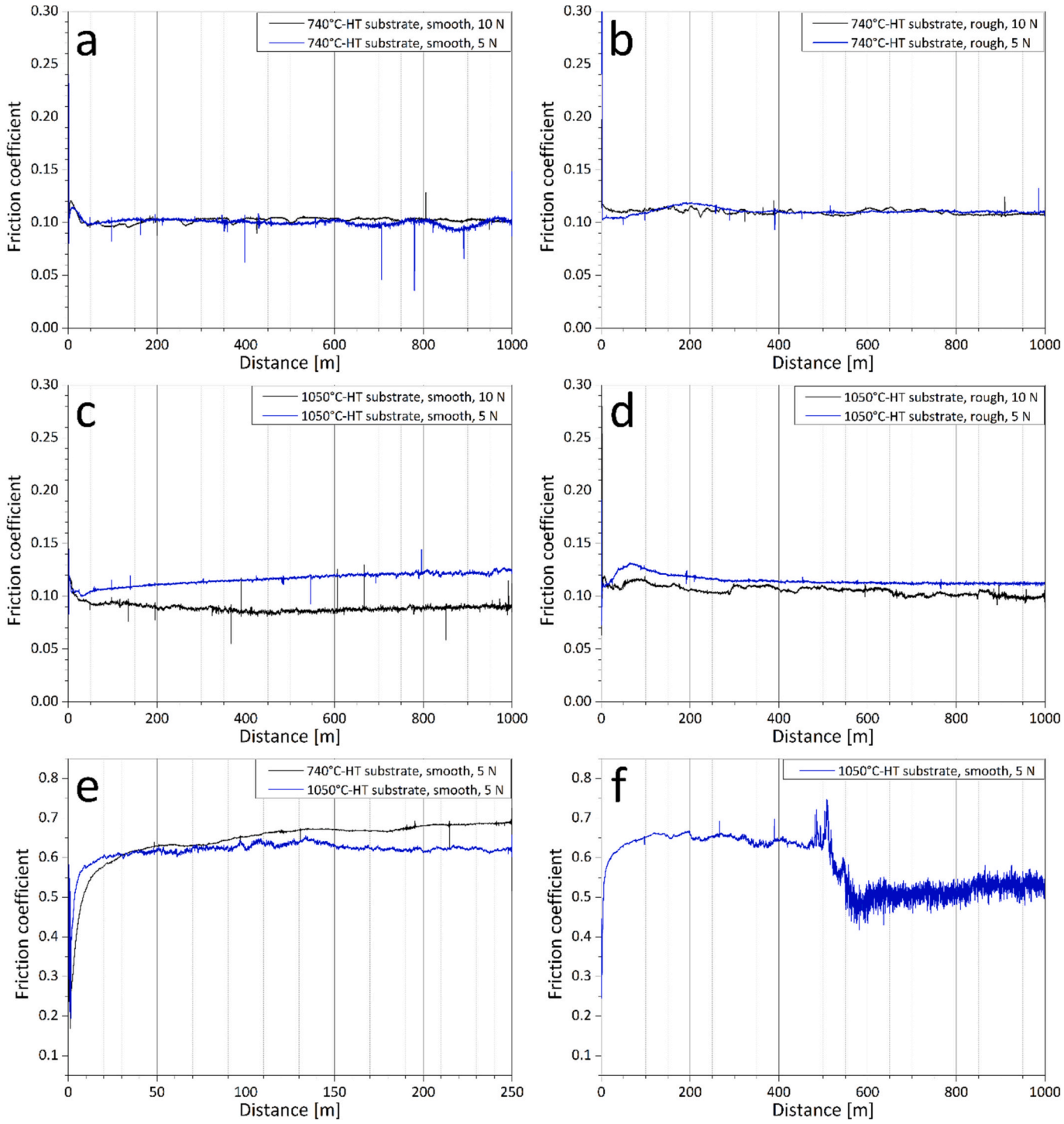

Fig. 10. Representative friction curves obtained during ball-on-disc tests: (a-d) DLC-based films deposited onto Ti64 substrates heat-treated at 740 °C (a – smooth substrate, b – rough substrate) and 1050 °C (c – smooth substrate, d – rough substrate), tested over a 1000 m distance; (e) AlCrN films onto smooth substrates under both heat-treatment conditions, tested over a 250 m distance; (f) the same AlCrN film onto a smooth substrate heat-treated at 1050 °C, tested over a sliding distance of 1000 m.

samples were retrieved after the test, during sliding some of this debris was likely sheared between the surfaces, as previously discussed by Scharf and Singer [70].

SEM micrographs (which were acquired on samples cleaned in an ultrasonic bath with acetone to remove the loose debris seen in Fig. 11a) confirm a very mild form of abrasion for the DLC coatings onto smooth substrates when tested at 5 N load (Fig. 13a, e). Occasional bright spots, which might indicate uncovering of the WC-C interlayer, were probably due to the removal of a few anomalously large clusters among those previously described in Fig. 2d.

On the rough substrates (Fig. 13b, f and d, h), by contrast, the WC-C interlayer was more systematically uncovered on the roughness crests, both at the same 5 N load and at 10 N load (also see the corresponding EDX spectra: Fig. 14c, d – spectra 1–3). From Fig. 13f and h, it looks like the removal of the DLC layer on the crests occurred by two mechanisms. On the one hand, because the real contact with the ball was localized on

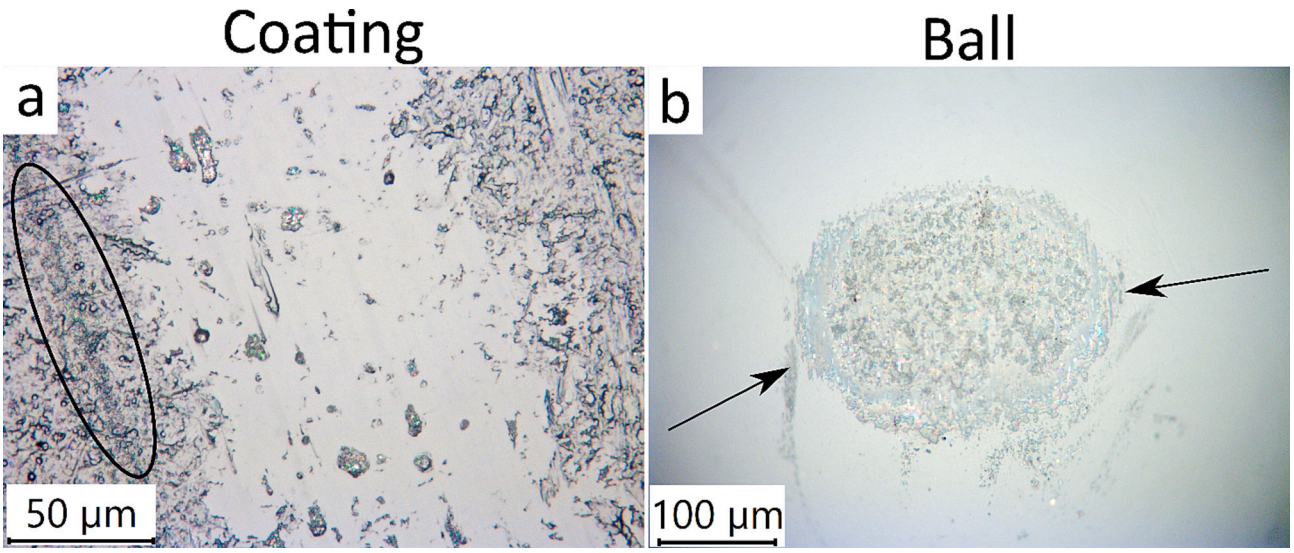

Fig. 11. Optical micrograph of the wear track produced on the DLC-based film deposited onto a smooth substrate heat-treated at 740 °C (a) and on the corresponding Al_2O_3 ball counterpart (b). The circle in panel (a) and the arrows in panel (b) indicate debris around the wear scar.

small areas on the crests, the DLC layer was progressively abraded at a higher rate than it happened on "smooth" substrates, until the underlying layer was exposed. On the other hand, several of these areas show signs of chipping and spallation, i.e. well before the DLC-based layer was gradually worn out, brittle failure happened. This was also the mechanism that likely occurred in each of the three uncovered areas marked for EDX spectroscopy in Fig. 14c. Cross-sectional views of the worn samples also confirm that the WC-C interlayer was exposed by either progressive wear (Fig. 15a – label 1) or brittle spallation (label 2). In other instances, spallation was confined within the DLC film and did not result in exposure of the interlayer (label 3 and detail in panel b). Very interestingly, the cracks deflected along an angled path in the WC-C interlayer (Fig. 15a, b: in particular, see the arrow in panel b) in the same way as was seen in the FIB sections after the VDI test (Section 3.2, Fig. 8).

It is interesting to try to explain why the ball-on-disc test was so much more sensitive to the substrate finishing than were the scratch test results discussed in Section 3.2. First, it is noted that possible discrepancies between scratch testing, VDI testing and ball-on-disc testing in rating the load-carrying ability of DLC-coated systems have already been found by Ronkainen et al. [14]. In the scratch tests, the comparatively much sharper (100 µm radius) tip always contacted the surface in a very small area, as Ronkainen et al. also discussed in the paper cited above. For example, applying Hertz's contact model for a 100 µm-radius diamond sphere (E = 1141 GPa, $\nu = 0.07$) pressed onto a flat surface with the elastic modulus of the present DLC samples (E ≈ 200 GPa, Table 5), the contact radius is computed to be around 14 µm at a load of 7 N (roughly corresponding to the L_{C2} values listed in Table 6). This computation is highly approximate, but it shows that the contact radius is comparable to the width of the roughness crests seen in Fig. 13b, f. Thus, highly localized contact occurred regardless of whether the films were deposited onto a smooth or rough substrate. Moreover, the scratch tester had a feedback system to control the normal load; therefore, it could adjust the load to avoid unwanted overloads on the crests of the rough surface.

By contrast, in the ball-on-disc test, the radius of the counterpart was more than one order of magnitude larger (1.5 mm). Thus, the contact radius during the test was correspondingly larger, as also noted by Ronkainen et al. [14]. Assuming E = 370 GPa, $\nu = 0.22$ for sintered alumina (see Section 2.4), a contact radius of about 35 µm is computed at 5 N load. Further, this is likely an underestimation because this calculation neglects the elastic deformation of the less stiff titanium alloy substrate (E ≈ 114 GPa [75]), as also explained previously in Section 2.4. Thus, multiple asperities were contacted by the ball at the same time, and the determining factor that controlled the coating's response was whether the real area of contact, which depends on the mechanical properties of the mating bodies and their surface roughness, was large enough to keep the asperities within an elastic deformation regime.

This can be assessed, to a first approximation, using the plasticity index (ψ) proposed by Greenwood and Williamson [76]:

$$\psi = (E^*/H)\sqrt{\sigma/R} \quad (1)$$

where:

H = hardness of the worn surface;

$E^* = \left(E_1^{*-1} + E_2^{*-1}\right)^{-1}$ = reduced plane-strain elastic modulus;

$E^*_{1,2} = E_{1,2}/\left(1-\nu^2_{1,2}\right)$ = plane-strain elastic moduli of the two mating surfaces, with $E_{1,2}$ = Young's moduli, $\nu_{1,2}$ = Poisson's ratios, and the subscripts 1 and 2 indicate the two different mating bodies;

σ = standard deviation of the height distribution of the "composite" surface profile, which coincides with the root mean square height Sq if the mean line of the profile is taken as the reference to define the height values, as it is in fact prescribed by the roughness measurement standards;

R = mean curvature radius of the asperities of the "composite" surface profile = 1/Spc.

Because the ball surface (Table 3) is much smoother than the coated samples (Table 2), the "composite" profile of the mating bodies practically coincides with that of the coating. Indeed, even compared to the "smooth" samples, the Sq and Spc values of the ball counterpart are almost one order of magnitude lower; thus, encompassing their effect on the "composite" surface profile would result in minimal changes. Therefore, the root mean square height Sq and arithmetic mean peak curvature Spc of the substrates (Table 2) can be used in Eq. (1). Note that the SEM micrographs in Fig. 13a, b, e, f, combined with the very short running-in stage of the friction curves in Fig. 10a-d, suggest that the additional roughness due to the surface clusters on the DLC films was smoothed down soon after the beginning of the test. Therefore, it is more appropriate to use the roughness of the substrates rather than that of the coated samples, where a slight increase in roughness would have been detected because of these clusters. With the mechanical properties ($E_{1,2}$ and $\nu_{1,2}$) of the DLC-based films and the alumina counterbody mentioned above, the plasticity index values listed in Table 8 are

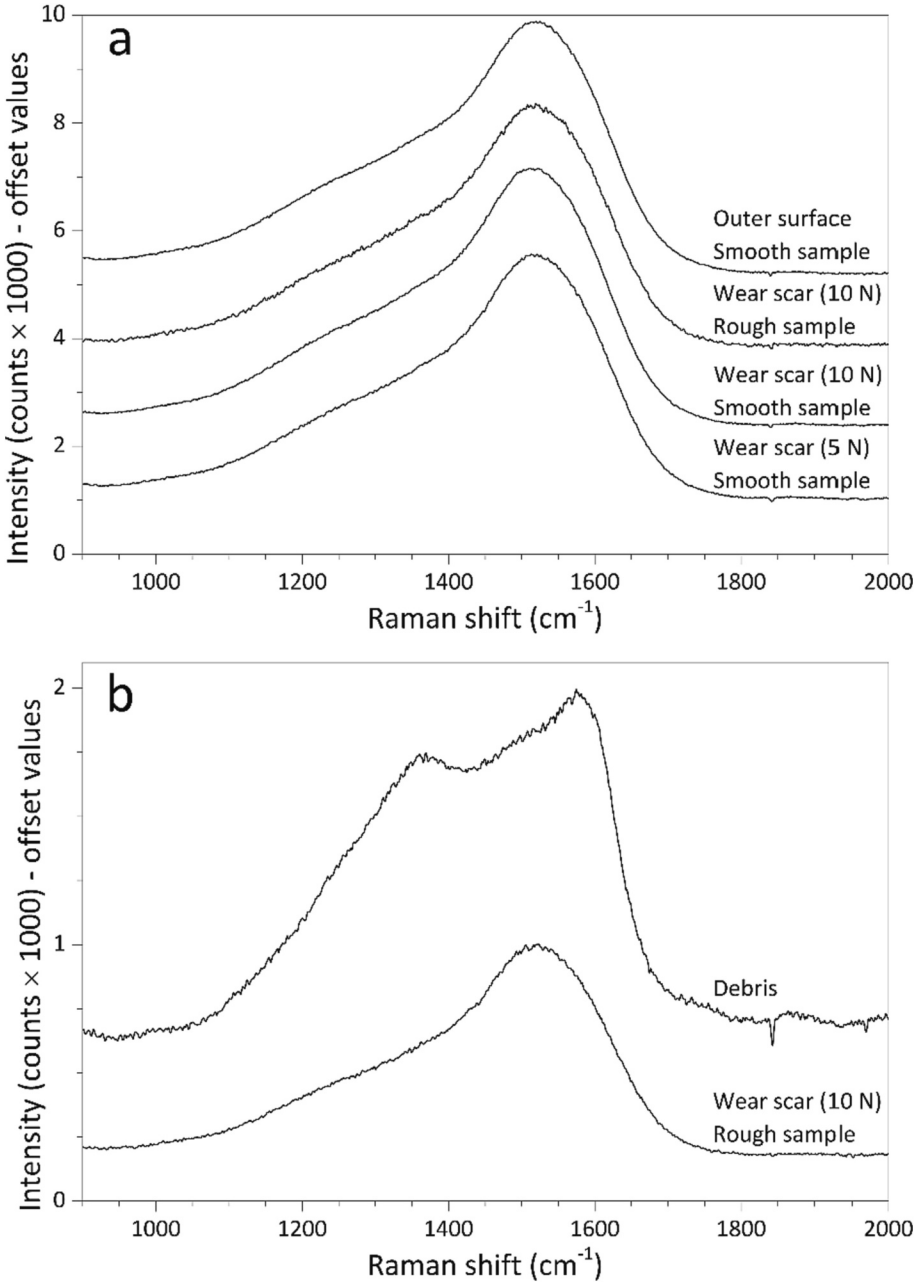

Fig. 12. Comparison between micro-Raman spectra acquired inside and outside the ball-on-disc wear tracks on the DLC-based films deposited onto smooth and rough Ti64 substrates heat-treated at 1050 °C (a), and between micro-Raman spectra acquired inside a wear track and on the debris along the track edges (b).

Table 7
Position of the G-band, ratio between the intensities of the D and G bands (I(D)/I(G)) and full width of the G band at half-maximum height (FWMH(G)) obtained by fitting the Raman spectra acquired on DLC-based coatings deposited on smooth substrates heat-treated at 1050 °C, inside and outside the ball-on-disc wear tracks obtained at 5 N and 10 N normal load.

	Normal load: 5 N load		Normal load: 10 N load	
	Wear scar	Outer area	Wear scar	Outer area
G-band position (cm^{-1})	1538.0 ± 0.8	1539.4 ± 0.5	1535.5 ± 1.6	1537.1 ± 0.5
I(D)/I(G)	0.58 ± 0.01	0.59 ± 0.01	0.61 ± 0.04	0.59 ± 0.01
FWHM(G) (cm^{-1})	195.3 ± 1.9	194.5 ± 1.1	193.0 ± 3.6	195.3 ± 1.3

obtained.

In general, the elastic limit is exceeded at all contacting asperities if $\psi > 1$ [76]. Therefore, the results in Table 8 show that, with a rough substrate, the DLC coating was well past the elasticity limit during the ball-on-disc test (Table 8). Due to the very limited plastic deformability of DLC, exceeding the elastic limit by such a conspicuous amount induced brittle fracture, which explains the behaviour seen in Fig. 13b, f. On the other hand, also considering the very approximate nature of these computations, it can be inferred that the smooth substrate provided a sufficiently large contact area to avoid systematic brittle fracture.

Increasing the load to 10 N, despite the absence of any significant variation in the specific wear rates (or even a slight decrease, Fig. 9), caused very small cracks even on the "smooth" substrate (Fig. 13c, g), again exposing the WC-C interlayer (see EDX spectra 1 and 2 in Fig. 14a, b). The plasticity index (Eq. (1)) is independent of the applied load,

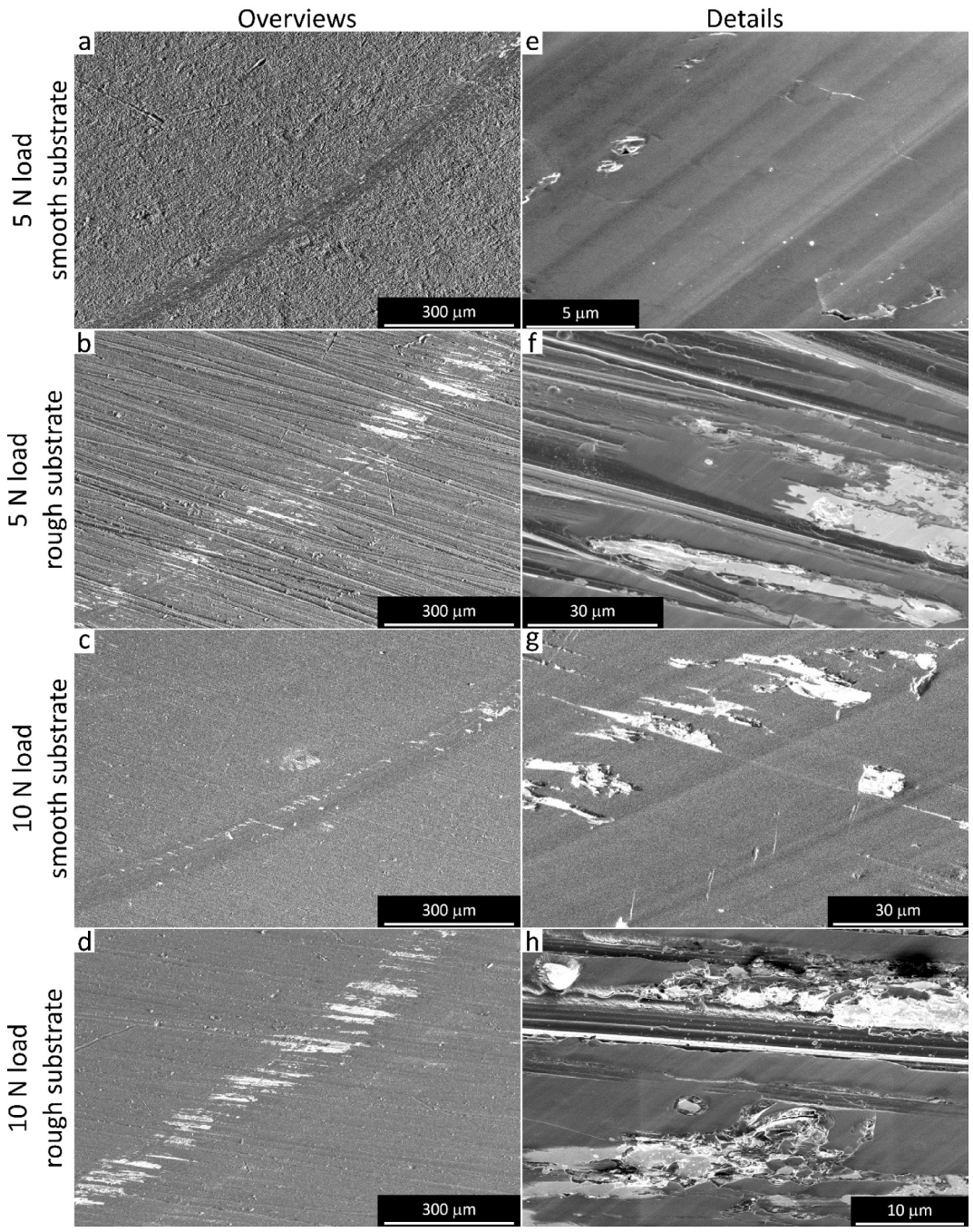

Fig. 13. SEM micrographs of the worn DLC surfaces after ball-on-disc testing: 5 N normal load with smooth (a, e) and rough (b, f) substrate heat-treated at 740 °C; 10 N normal load with smooth substrate heat-treated at 1050 °C (c, g) and rough substrate heat-treated at 740 °C (d, h) – general views (a-d) and details (e-h).

because to a first approximation the real contact pressure is independent of the applied normal load in both the elastic and plastic contact regime. However, another factor becomes relevant: the elastoplastic properties' mismatch between the coating and the substrate, which became more relevant in tests at 10 N load than at 5 N because the sub-surface stress peak moved to a greater depth and increased in magnitude, thus eliciting an increasingly large deformation in the substrate. Even if the substrate remained in an elastic deformation regime, its lower elastic modulus in comparison to the DLC-based film (≈114 GPa for the substrate vs. ≈200 GPa for the film, as specified above) means that the coating was subjected to a concentration of bending stresses as coating and substrate deformed together under the applied load. Such additional stress was compounded with the micro-scale contact stresses and thus triggered some brittle fracture.

Clearly, with a rough substrate under 10 N load, the effect was even more magnified; thus, brittle fracture happened more extensively than at 5 N load (Fig. 13d, h), resulting in an approximately linear increase in the overall wear volume that means an approximately constant specific wear rate, as noted previously.

3.3.3. *Wear mechanisms: AlCrN films*

As mentioned in Section 3.3.1, the tribological response of the AlCrN film differed much from that of the DLC-based ones. First of all, the AlCrN film did not withstand the higher normal load of 10 N and/or the use of a "rough" substrate, delaminating after just a few metres: Fig. 16c and d accordingly show deep ploughing and cutting grooves in the

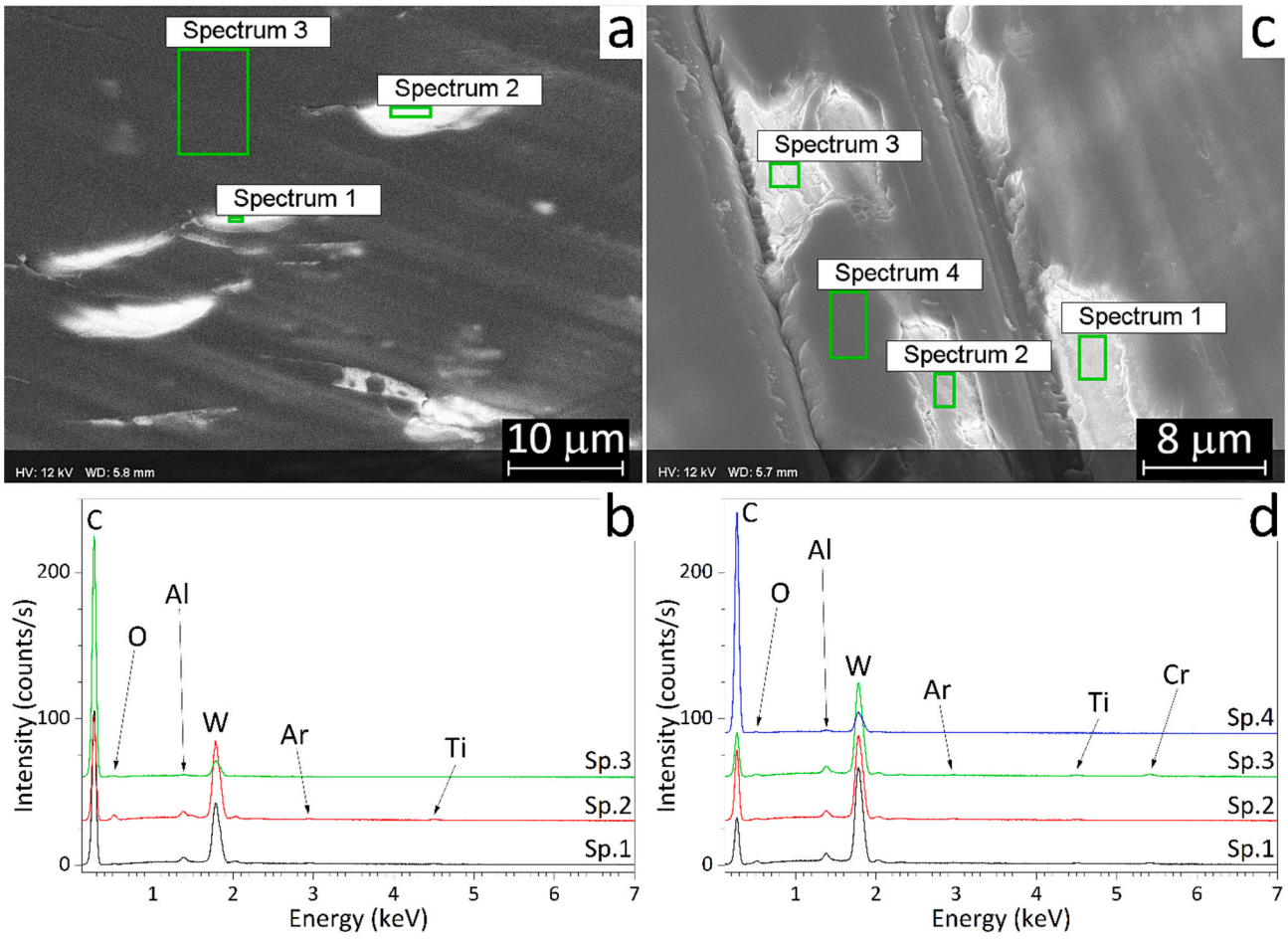

Fig. 14. SEM micrographs of the worn surfaces of the DLC films deposited onto a smooth substrate heat-treated at 1050 °C, 10 N load (a), and onto a rough substrate heat-treated at 1050 °C, 5 N load (c), with corresponding EDX spectra (b, d).

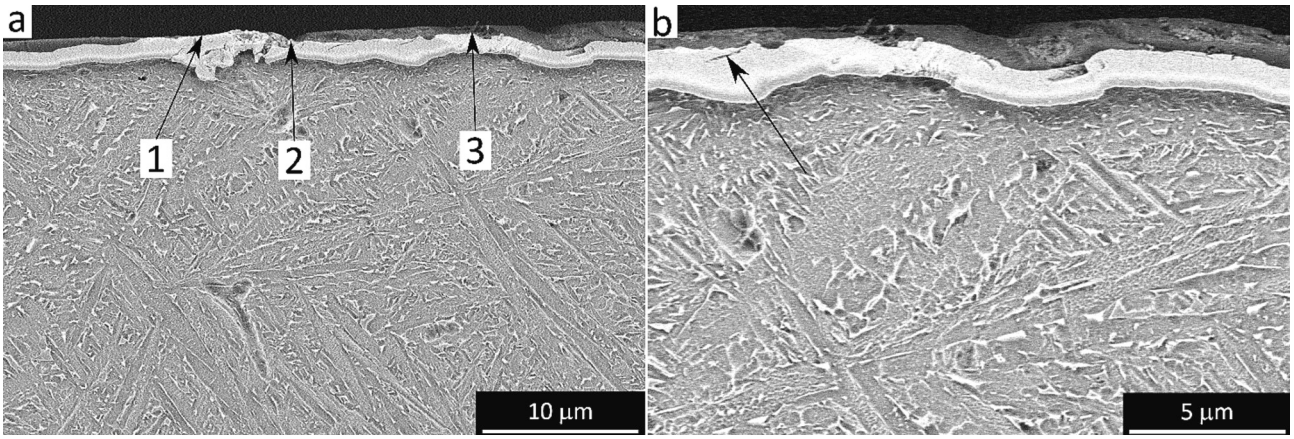

Fig. 15. Cross-sectional SEM micrographs of the DLC-based film deposited onto the rough substrate heat-treated at 1050 °C after ball-on-disc testing at 10 N load: overview (a) and detail (b). Label 1 = progressive wear of the DLC top layer uncovers the WC-C interlayer; 2 = brittle fracture led to complete spallation of the DLC top layer; 3 = brittle fracture with partial spallation of the DLC top layer. The arrow in panel (b) shows a microcrack deflecting and finally stopping in the WC-C interlayer.

uncovered substrate at the end of a test run for 250 m at 5 N load with a "rough" substrate.

On the other hand, the AlCrN films deposited onto a "smooth" substrate survived a 250 m-long test at 5 N load with very low specific wear rates, of the same order of those on the DLC films. Accordingly, Fig. 17a and b show a very shallow wear scar, partly covered by a film of debris with a darker contrast. The scar is so shallow that, in optical micrographs (Fig. 16a), it would be almost indistinguishable from the surrounding material, were it not for the distinctive colours of the debris film (possibly partly due to interference phenomena). The detail in Fig. 17b especially shows an accumulation of such debris in the dales of the surface, e.g. residual dales from deep grinding grooves that were not

Table 8
Plasticity index (ψ) values computed for coatings deposited onto smooth and rough substrates.

	DLC-based coating		AlCrN coating	
	Smooth substrate	Rough substrate	Smooth substrate	Rough substrate
Plasticity index ψ	1.1	6.4	1.3	7.3

removed completely by the finer grinding steps (see the negative Ssk value in Table 2).

The optical micrograph of Fig. 16b shows that the worn surface of the ball is also covered by a thick layer of debris. In Fig. 17b, sub-micrometric "rolls" appear (see arrows). They consist of secondary debris: rolls were formed by the extrusion of thin sheets from the debris clusters that adhered to the surface, and were curled up under the large shear stress exerted as they were being extruded. Their formation is a known phenomenon during sliding wear of ceramic materials [77].

EDX analyses (Fig. 17c, d: spectra 2 and 3) show an oxygen peak in the spectra of the debris film, suggesting that it was at least partly tribo-oxidized. Micro-Raman spectra (Fig. 18) acquired on the coloured debris seen in Fig. 16a, however, contain prominent peaks of AlCrN, indicating that tribo-oxidation of the debris was not complete. Additional peaks around 860 cm^{-1} and 1005 cm^{-1} can be interpreted as being produced by a mixture of Cr^{3+} and Cr^{6+} oxides/hydroxides (or also by compounds where Cr is in an intermediate oxidation state), and by Cr^{6+} compounds, respectively [77]. These are the compounds resulting from tribo-oxidation. The formation of Cr oxides with various valence states in the tribo-oxidized debris produced during sliding wear of AlCrN films is consistent with [63].

The removal of the AlCrN film onto "smooth" substrates over longer sliding distances was thus not due to progressive wear: the mild wear rates shown in Fig. 9, confirmed by the shallow groove in Fig. 17a-c and Fig. 16a, would have allowed the film to survive the same distance of 1000 m as the DLC-based films. Removal was likely the consequence of fatigue accumulation leading to cracking and spallation. Accordingly, Fig. 17e and f, which show the surface of a worn AlCrN sample where spallation started shortly before the end of the 250 m-long test, highlight a brittle fracture running along intercolumnar boundaries (see the circled area in panel f). Note that due to the anomalously early onset of fatigue failure, the result of this test was not included in the computation of the average specific wear rates of Fig. 9.

The previously cited literature studies where unidirectional ball-on-disc tests were carried out with AlCrN films onto cemented carbide substrates [48,71,73,74] never reported the occurrence of fatigue spallation, but it should also be noted that the sliding distance and track radii employed in [71,73,74] were such that the overall number of revolutions of the coated disc (i.e. the number of fatigue cycles experienced by every point on the coated surface within the wear track) was lower than in the present test. Therefore, it is possible that the tests did not last long enough to see fatigue spallation, also considering that, although the normal load in the cited papers was the same as in the present tests, i.e. 5 N, the ball counterparts had larger diameter. Hence, the nominal contact pressure was lower. Only in [48] was the number of revolutions significantly higher than in the present tests: almost 40,000 revolutions were performed, against the 9925 revolutions of the present, 250 m-long test. Since no spallation was reported in [48], we can infer that the poorer mechanical support provided by the Ti-6Al-4V substrates promoted this kind of fatigue spallation compared to a harder and elastically stiffer cemented carbide, although the initial nominal contact pressure used in [48] was lower than in our tests (the applied load was 5 N and the ball material was Al_2O_3, as in the present work, but the ball diameter was 6 mm instead of 3 mm).

Nonetheless, the present wear test results also indicate that, just as in the case of the DLC-based films, the performances of the AlCrN coatings

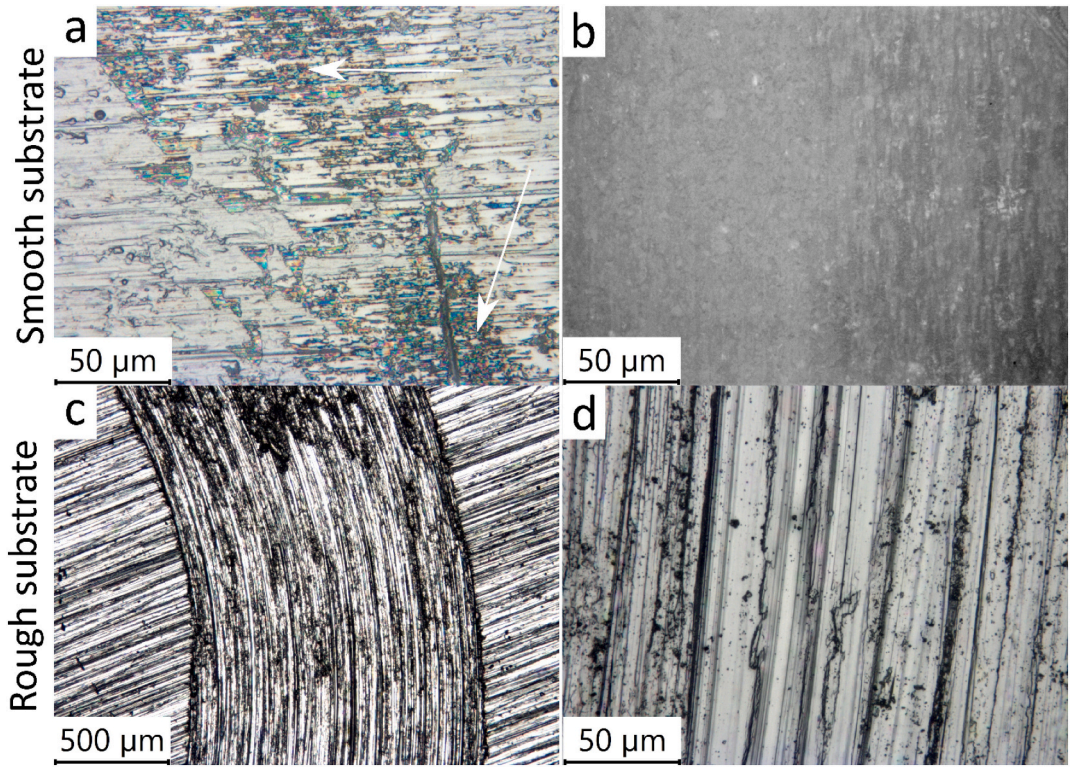

Fig. 16. Optical micrographs of the wear tracks produced at 5 N normal load on the AlCrN film deposited onto a "smooth" substrate heat-treated at 740 °C (a), with the corresponding Al_2O_3 counterpart (b), and onto a "rough" substrate heat-treated at the same temperature (c), with a magnified detail (d). The arrows in panel (a) indicate a tribolayer on the wear scar.

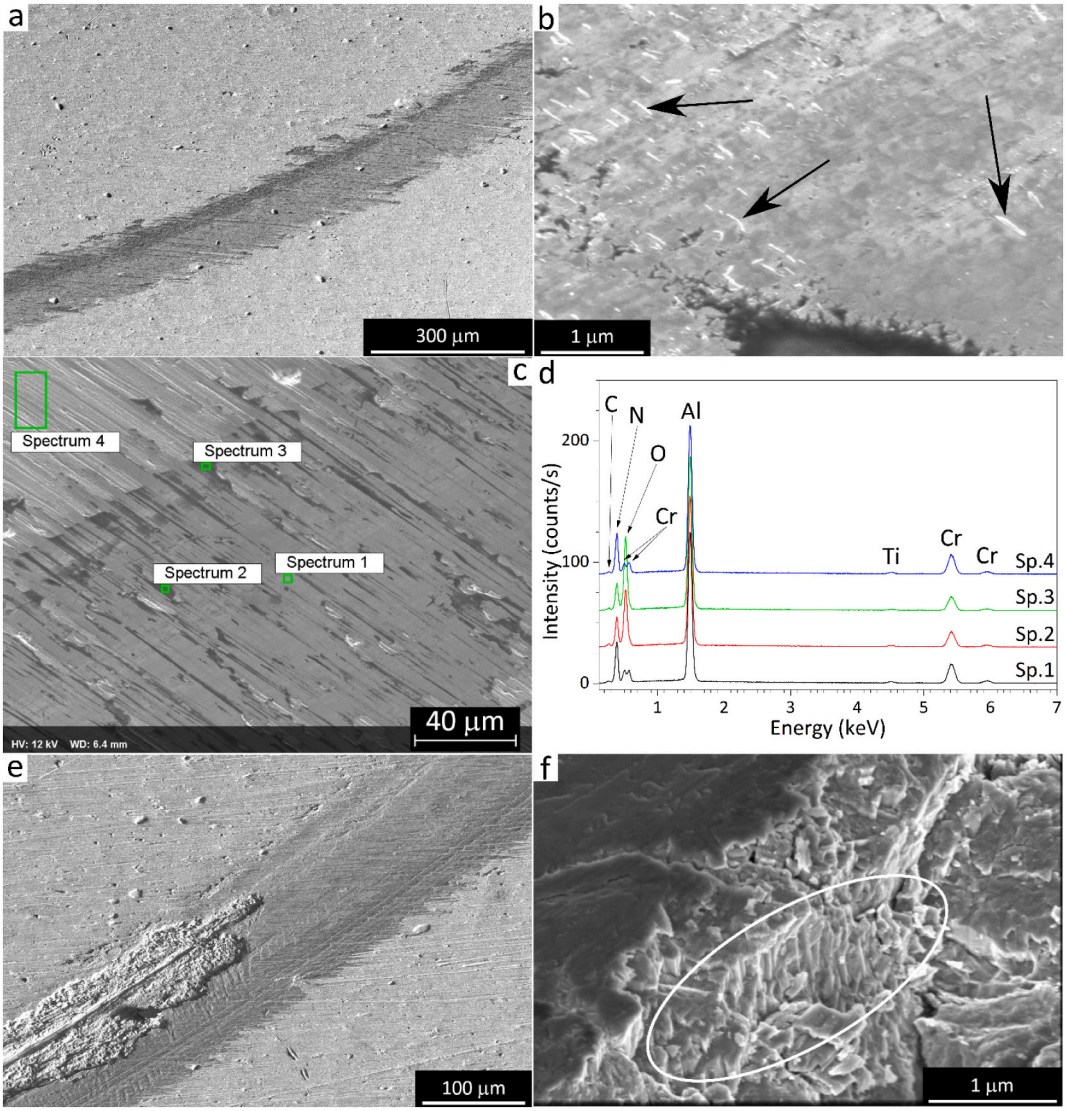

Fig. 17. Ball-on-disc wear scars on the AlCrN films deposited onto "smooth" substrates heat-treated at 740 °C: SEM micrographs (a: overview, b: detail, c: backscattered-electrons view) with corresponding EDX spectra (d); and SEM micrographs of a sample where spallation initiated shortly before the end of the 250 m-long test (e: overview; f = detail; circle = intercolumnar fracture).

deposited onto additively manufactured substrates are comparable to or competitive with those on conventionally manufactured parts.

Interestingly, the spallation crack that propagated across the film was deflected longitudinally next to the substrate interface (Fig. 19), just as it did in the scratch and VDI tests. Hence, the failure modes seen in those scratch tests were truly representative of actual spallation modes encountered under severe service conditions. We indeed found this to be true for both the DLC-based films (see the previous considerations in Section 3.3.2) and the AlCrN ones.

The almost instantaneous delamination of the AlCrN films on the rough substrates, as well as the fatigue failure of those on smooth substrates as discussed above, cannot be ascribed to poorer adhesion of AlCrN compared to the DLC-based film. In fact, their scratch and VDI test results were analogous (Section 3.2). Therefore, failure must be ascribed to a more severe stress state to which the AlCrN films were subjected during the ball-on-disc test, compared with the DLC-based ones. On the one hand, the AlCrN coating has ≈1.5 times higher hardness but >2 times higher elastic modulus compared to the DLC-based one (Table 5), i.e. it has lower H/E ratio. Therefore, higher plasticity index values are computed onto both smooth and rough substrates (Table 8). Moreover, a film with lower hardness-to-modulus ratio is even more sensitive to the stress peaks due to elastic or plastic bending of the substrate under the applied load (as discussed previously). On the other hand, the higher friction coefficient indicates that a larger friction force, resulting in in-plane normal stress and out-of-plane shear stress components, was exerted onto the AlCrN films during the sliding wear test. Thus, the highly stressed AlCrN films tended to accumulate contact fatigue and spall.

It is indeed clear that the partly oxidized tribo-film seen in Fig. 17a-d was not conducive to low friction (Figs. 9 and 10e, f). Perhaps, the fact that the debris filled the surface dales (Fig. 17b) had a negative effect, because it increased the real area of contact with the counterbody. Indeed, for a given strength of the adhesive interactions between the mating surfaces at their contact points (τ_m), an increase in the real area of contact (A_r) results in a larger overall tangential force ($F_T = \tau_m \times A_r$) to keep the bodies in relative motion [78]. Interaction with humidity might also have made this debris "sticky", so that the τ_m values that were produced as the debris film on the sample interacted with the counterface were high. Accordingly, Souza et al. [79] showed that the surface energy of AlCrN is dominated by a polar component of non-negligible magnitude (~20 mJ/m^2), which makes it chemically affine to polar water molecules. Likewise, it is expected that the chromium-based

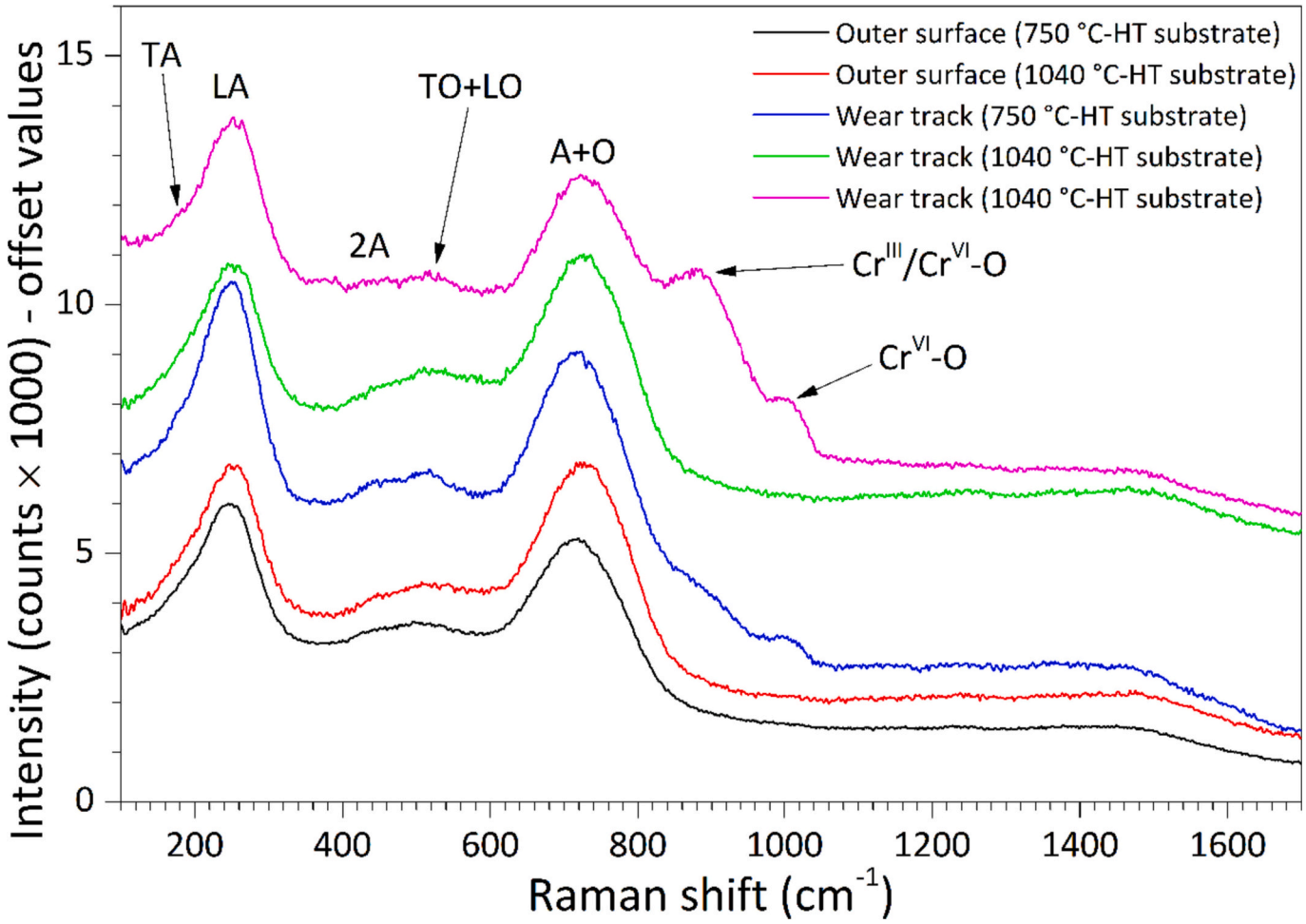

Fig. 18. Micro-Raman spectra acquired on the AlCrN films deposited onto smooth substrates heat-treated at 740 °C and 1050 °C, inside and outside the wear tracks.

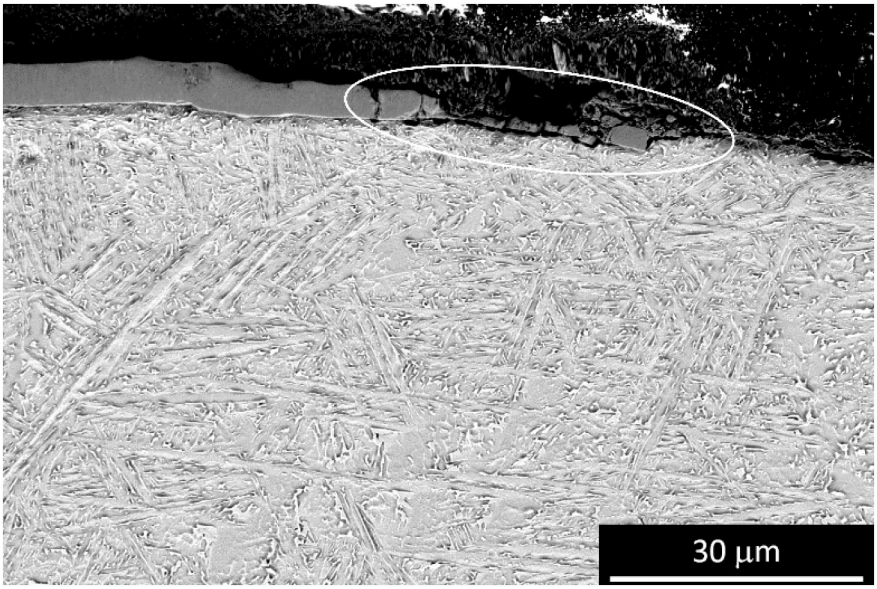

Fig. 19. Cross-sectional SEM micrograph of the spallation area in the "anomalous" ball-on-disc test of an AlCrN coating onto the smooth, 740 °C-treated substrate that started to fail shortly before 250 m.

oxides found by Raman spectroscopy, due to their chemical nature, have a dominant polar surface energy component. Thus, both the non-oxidized and the tribo-oxidized constituents of the debris layer were likely to interact with humidity. Interestingly, Liew et al. [46] found higher friction coefficients when ball-on-disc testing of AlCrN was carried out in humid air, compared to tests in vacuum. This lends some support to the above considerations on the role of humidity, although Liew et al. employed different test conditions (with a sintered WC-Co counterpart instead of an Al_2O_3 one) and did not analyse the tribological mechanisms to identify the causes for those different friction responses.

As a final note, it is seen from Fig. 9 that the heat treatment condition of the substrate probably had a small but perceivable effect on the specific wear rate of the AlCrN film, unlike with the DLC-based ones. Namely, the softer substrate treated at 1050 °C resulted in a higher specific wear rate. Due to the more severe stress state to which the AlCrN films were subjected because of their unfavourable H/E ratio and the higher friction coefficient they produced, a further stress increase because of plastic deformation of a softer substrate under a higher normal load might have had a more pronounced effect than it did with the DLC-based coatings.

4. Conclusions

In this work, we studied the deposition of thin-film coatings onto Laser-Powder Bed Fusion (L-PBF) Ti-6Al-4V alloy substrates. Specifically, the focus was on how the post-process heat treatment of the substrate (below or above the β-transus temperature) and its surface finish (a "rough" or a "smooth" surface, obtained by grinding with different grit sizes) affected the adhesion and sliding wear performance of two thin-film coatings: a DLC-based coating obtained by a combined PVD + PE-CVD technique and a PVD AlCrN coating.

The results allowed to draw the following conclusions:

- The films exhibited better scratch adhesion to the harder substrates treated below the β-transus, because these substrates offered better mechanical support.

  On the other hand, the roughness of the substrate had little effect on scratch adhesion. Probably, the small curvature radius of the indenter resulted in a contact area so small, that there was not much difference between its extension with either a "smooth" or a "rough" substrate surface.

  There was also little difference between the scratch adhesion of the AlCrN and DLC-based films.
- In ball-on-disc adhesion tests, on the other hand, major differences emerged between the AlCrN and DLC-based films and, for each type of coating, the substrate roughness was more influential than its heat-treatment condition.
- The DLC-based film on a "smooth" substrate survived a 1000 m-long ball-on-disc wear test at a load of 5 N with no crack formation. Mild polishing wear and the formation of a layer of graphitized debris resulted in a low specific wear rate of $\sim 10^{-7}$ $mm^3/(N \bullet m)$ and a friction coefficient around 0.1 against an Al_2O_3 counterpart. Microcracking and chipping of the film off the roughness crests happened with a "rough" substrate finish and/or with a higher normal load of 10 N, although there was little or no measurable effect on the specific wear rate and the friction coefficient.
- The AlCrN film on a "smooth" substrate delaminated because of contact fatigue at a load of 5 N after sliding distances of 250–450 m, though it retained a mild specific wear rate of $\sim 2–4 \times 10^{-7}$ $mm^3/(N \bullet m)$ up to 250 m of sliding. A chromium oxide/hydroxide-based tribofilm was developed on the AlCrN film, but it did not possess the same solid-lubrication capability as the graphitized DLC debris. "Rough" substrates and/or a load of 10 N resulted in almost immediate spallation of the AlCrN film.
- The tribological response of the DLC-based film was insensitive to the substrate heat treatment condition. By contrast, slightly higher wear was observed with the AlCrN film onto the softer substrate treated above the β-transus.
- The different response of DLC-based and AlCrN films can be interpreted through the plasticity index, which, accounting for both the H/E ratio and the surface roughness, indicates whether the elastic limit is exceeded at the real contact points. Whilst this value is around 1 for the DLC-based film onto the "smooth" substrate, it is higher for the AlCrN film and, in both cases, it increases substantially when the films are deposited onto the "rough" substrate. Thus, the plasticity index can be an especially useful parameter for a preliminary estimation of the suitability of the contact conditions.

  The plasticity index is independent of the normal load, but an increase from 5 N to 10 N resulted in a greater depth of the contact stress maximum, implying even greater deformation of the Ti-6Al-4V substrate. Thus, further stress was imposed on the films, with AlCrN suffering the most severe damage because of its lower elastic compliance (lower H/E ratio).
- Overall, it is concluded that thin-film coatings can be deposited onto L-PBF Ti-6Al-4V substrates with performances analogous to those known for conventionally machined parts, but the surface finishing and, to a minor extent, the heat-treatment condition of the substrate must be taken into account when considering the type of coating and the admissible contact conditions. Future developments of this work might include exploring a wider range of surface finishes and studying the tribological response of the AlCrN-coated systems at higher temperatures.

CRediT authorship contribution statement

Emanuele Ghio: Conceptualization, Methodology, Formal analysis, Investigation, Data curation, Writing – review & editing. **Giovanni Bolelli:** Conceptualization, Methodology, Investigation, Formal analysis, Data curation, Writing – original draft, Supervision. **Alessandro Bertè:** Methodology, Resources, Writing – review & editing. **Emanuela Cerri:** Conceptualization, Methodology, Resources, Writing – review & editing, Supervision.

Declaration of competing interest

The authors declare the following financial interests/personal relationships which may be considered as potential competing interests: Emanuele Ghio reports financial support was provided by Italian Ministry of University and Research. Alessandro Berte reports a relationship with Lafer S.p.A. that includes: employment.

Data availability

Data will be made available on request.

Acknowledgements

Many thanks to Mr. Daniele Buzzega for his contribution to the experimental activities and to Mr. Paolo Colombi (Lafer S.p.A.) for the assistance with coatings' deposition.

The project was funded under the National Recovery and Resilience Plan (NRRP), Mission 4, Component 2, Investment 1.5. – Call for tender No. 3277 of 30/12/2021 of Italian Ministry of University and Research funded by European Union – NextGenerationEU.

References

[1] A. Gebhardt, Applications, in: Understanding Additive Manufacturing, Carl Hanser Verlag GmbH & Co. KG, München, 2011, pp. 65–101, https://doi.org/10.3139/9783446431621.003.

[2] J.-P. Kruth, S. Dadbakhsh, B. Vrancken, K. Kempen, J. Vleugels, J. Van Humbeeck, Additive manufacturing of metals via selective laser melting: process aspects and material developments, in: T.S. Srivatsan, T.S. Sudarshan (Eds.), Additive Manufacturing: Innovations, Advances, and Applications, CRC Press, Boca Raton, FL, USA, 2016, pp. 69–99.

[3] B. Dutta, F.H. Froes, Markets, applications, and costs, in: Additive Manufacturing of Titanium Alloys, Elsevier, 2016, pp. 61–73, https://doi.org/10.1016/B978-0-12-804782-8.00006-9.

[4] B. Dutta, F.H. Froes, The additive manufacturing of titanium alloys, in: Additive Manufacturing of Titanium Alloys, Elsevier, 2016, pp. 1–10, https://doi.org/10.1016/B978-0-12-804782-8.00001-X.

[5] M.J. Donachie, Titanium: a technical guide, 2nd edition | introduction to selection of titanium alloys, ASM Int. 180 (2000) 5–11.

[6] Fundamental aspects, in: G. Lütjering, J.C. Williams (Eds.), Titanium, Springer, Berlin, Germany, 2007, pp. 15–52, https://doi.org/10.1007/978-3-540-73036-1_2.

[7] M. Peters, J. Hemptenmacher, J. Kumpfert, C. Leyens, Structure and properties of titanium and titanium alloys, in: Titanium and Titanium Alloys, Wiley-VCH Verlag GmbH & Co. KGaA, Weinheim, FRG, 2005, pp. 1–36, https://doi.org/10.1002/3527602119.ch1.

[8] B. Dutta, F.H. Froes, Microstructure and mechanical properties, in: Additive Manufacturing of Titanium Alloys, Elsevier, 2016, pp. 41–50, https://doi.org/10.1016/B978-0-12-804782-8.00004-5.

[9] S. Sun, M. Brandt, M. Easton, Powder bed fusion processes, in: M. Brandt (Ed.), Laser Additive Manufacturing, Elsevier - Woodhead Publishing, 2017, pp. 55–77, https://doi.org/10.1016/B978-0-08-100433-3.00002-6.

[10] L. Thijs, F. Verhaeghe, T. Craeghs, J. Van Humbeeck, J.-P. Kruth, A study of the microstructural evolution during selective laser melting of Ti–6Al–4V, Acta Mater. 58 (2010) 3303–3312, https://doi.org/10.1016/j.actamat.2010.02.004.

[11] S.A. Etesami, B. Fotovvati, E. Asadi, Heat treatment of Ti-6Al-4V alloy manufactured by laser-based powder-bed fusion: process, microstructures, and mechanical properties correlations, J. Alloys Compd. 895 (2022), 162618, https://doi.org/10.1016/j.jallcom.2021.162618.

[12] B. Vrancken, L. Thijs, J.-P. Kruth, J. Van Humbeeck, Heat treatment of Ti6Al4V produced by selective laser melting: microstructure and mechanical properties, J. Alloys Compd. 541 (2012) 177–185, https://doi.org/10.1016/j.jallcom.2012.07.022.

[13] S. Cecchel, D. Ferrario, G. Cornacchia, M. Gelfi, Development of Heat Treatments for Selective Laser Melting Ti6Al4V Alloy: Effect on Microstructure, Mechanical Properties, and Corrosion Resistance, Advanced Engineering Materials 22, 2020, p. 2000359, https://doi.org/10.1002/adem.202000359.

[14] H. Ronkainen, J. Koskinen, S. Varjus, K. Holmberg, Load-carrying capacity evaluation of coating/substrate systems for hydrogen-free and hydrogenated diamond-like carbon films, Tribol. Lett. 6 (1999) 63–73, https://doi.org/10.1023/A:1019107622768.

[15] C.T. Wang, T.J. Hakala, A. Laukkanen, H. Ronkainen, K. Holmberg, N. Gao, R.J. K. Wood, T.G. Langdon, An investigation into the effect of substrate on the load-bearing capacity of thin hard coatings, J. Mater. Sci. 51 (2016) 4390–4398, https://doi.org/10.1007/s10853-016-9751-8.

[16] K.G. Budinski, Tribological properties of titanium alloys, Wear 151 (1991) 203–217, https://doi.org/10.1016/0043-1648(91)90249-T.

[17] G. Straffelini, Materials for tribology, in: Friction and Wear - Methodologies for Design and Control, Springer International Publishing, Cham, Switzerland, 2015, pp. 159–199, https://doi.org/10.1007/978-3-319-05894-8_6.

[18] N. Chelliah, S.V. Kailas, Synergy between tribo-oxidation and strain rate response on governing the dry sliding wear behavior of titanium, Wear 266 (2009) 704–712, https://doi.org/10.1016/j.wear.2008.08.011.

[19] A. Jayachandran, S.V. Kailas, Evolution of wear debris morphology during dry sliding of Ti–6Al–4V against SS316L under ambient and vacuum conditions, Wear 456–457 (2020), 203378, https://doi.org/10.1016/j.wear.2020.203378.

[20] S.V. Kailas, S.K. Biswas, The role of strain rate response in plane strain abrasion of metals, Wear 181–183 (1995) 648–657, https://doi.org/10.1016/0043-1648(95)90181-7.

[21] A. Bloyce, P.H. Morton, T. Bell, Surface engineering of titanium and titanium alloys, in: Surface Engineering, ASM International, 1994, pp. 835–851, https://doi.org/10.31399/asm.hb.v05.a0001311.

[22] J. Fontaine, C. Donnet, A. Erdemir, Fundamentals of the tribology of DLC coatings, in: C. Donnet, A. Erdemir (Eds.), Tribology of Diamond-like Carbon Films, Springer US, Boston, MA, 2008: pp. 139–154. doi:https://doi.org/10.1007/978-0-387-49891-1_5.

[23] K. Holmberg, A. Laukkanen, H. Ronkainen, K. Wallin, S. Varjus, A model for stresses, crack generation and fracture toughness calculation in scratched TiN-coated steel surfaces, Wear 254 (2003) 278–291, https://doi.org/10.1016/S0043-1648(02)00297-1.

[24] W. Tillmann, N.F. Lopes Dias, D. Kokalj, D. Stangier, M. Hein, K.-P. Hoyer, M. Schaper, D. Gödecke, H. Oltmanns, J. Meißner, Tribo-functional PVD thin films deposited onto additively manufactured Ti6Al7Nb for biomedical applications, Mater. Lett. 321 (2022), 132384, https://doi.org/10.1016/j.matlet.2022.132384.

[25] A. Woźniak, M. Adamiak, G. Chladek, M. Bonek, W. Walke, O. Bialas, The influence of hybrid surface modification on the selected properties of CP titanium grade II manufactured by selective laser melting, Materials 13 (2020) 2829, https://doi.org/10.3390/ma13122829.

[26] M. Hein, N.F. Lopes Dias, D. Kokalj, D. Stangier, K.-P. Hoyer, W. Tillmann, M. Schaper, On the influence of physical vapor deposited thin coatings on the low-cycle fatigue behavior of additively processed Ti-6Al-7Nb alloy, Int. J. Fatigue 166 (2023), 107235, https://doi.org/10.1016/j.ijfatigue.2022.107235.

[27] J.C. Colombo-Pulgarín, A.J. Sánchez Egea, D.J. Celentano, D.M. Krahmer, V. Martynenko, N. López de Lacalle, Mechanical and chemical characterisation of TiN and AlTiSiN coatings on a LPBF processed IN718 substrate, Materials 14 (2021) 4626, https://doi.org/10.3390/ma14164626.

[28] W. Tillmann, N.F. Lopes Dias, D. Stangier, C. Schaak, S. Höges, Coatability of diamond-like carbon on 316L stainless steel printed by binder jetting, Addit. Manuf. 44 (2021), 102064, https://doi.org/10.1016/j.addma.2021.102064.

[29] N.V. Lezhnin, A.V. Makarov, V.P. Kuznetsov, A.B. Vladimirov, P.A. Skorynina, V. A. Sirosh, Adhesion strength of Ti1-xCx – DLC multilayer nanocomposite thin films coated by ion-plasma deposition on martensitic stainless steel produced by selective laser melting followed by plasma-nitriding and burnishing, J. Phys. Conf. Ser. 2064 (2021), 012082, https://doi.org/10.1088/1742-6596/2064/1/012082.

[30] J. Ni, F. Liu, G. Yang, G.-H. Lee, S.-M. Chung, I.-S. Lee, C. Chen, 3D-printed Ti6Al4V femoral component of knee: improvements in wear and biological properties by AIP TiN and TiCrN coating, J. Mater. Res. Technol. 14 (2021) 2322–2332, https://doi.org/10.1016/j.jmrt.2021.07.143.

[31] M. Ranuša, P. Čípek, M. Vrbka, D. Paloušek, I. Křupka, M. Hartl, Tribological behaviour of 3D printed materials for small joint implants: a pilot study, J. Mech. Behav. Biomed. Mater. 132 (2022), 105274, https://doi.org/10.1016/j.jmbbm.2022.105274.

[32] W. Tillmann, N.F. Lopes Dias, D. Stangier, C. Schaak, S. Höges, Heat treatment of binder jet printed 17–4 PH stainless steel for subsequent deposition of tribo-functional diamond-like carbon coatings, Mater. Des. 213 (2022), 110304, https://doi.org/10.1016/j.matdes.2021.110304.

[33] H. Li, Z.W. Chen, M. Ramezani, Wear behaviours of PVD-TiN coating onTi-6Al-4V alloy processed by laser powder bed fusion or conventionally processed, Int. J. Adv. Manuf. Technol. 113 (2021) 1389–1399, https://doi.org/10.1007/s00170-021-06714-2.

[34] I. Gibson, D. Rosen, B. Stucker, M. Khorasani, Post-processing, in: Additive Manufacturing Technologies, Springer International Publishing, Cham, 2021, pp. 457–489, https://doi.org/10.1007/978-3-030-56127-7_16.

[35] M. Leary, Surface roughness optimisation for selective laser melting (SLM), in: M. Brandt (Ed.), Laser Additive Manufacturing, Elsevier - Woodhead Publishing, Duxford, UK, 2017, pp. 99–118, https://doi.org/10.1016/B978-0-08-100433-3.00004-X.

[36] J.C. Fox, S.P. Moylan, B.M. Lane, Effect of process parameters on the surface roughness of overhanging structures in laser powder bed fusion additive manufacturing, Procedia CIRP 45 (2016) 131–134, https://doi.org/10.1016/J.PROCIR.2016.02.347.

[37] D.A. Lesyk, S. Martinez, B.N. Mordyuk, V.V. Dzhemelinskyi, G.I. Prokopenko Lamikiz, Post-processing of the Inconel 718 alloy parts fabricated by selective laser melting: effects of mechanical surface treatments on surface topography, porosity, hardness and residual stress, Surf. Coat. Technol. 381 (2020), 125136, https://doi.org/10.1016/J.SURFCOAT.2019.125136.

[38] K. Holmberg, A. Matthews, H. Ronkainen, Coatings tribology—contact mechanisms and surface design, Tribol. Int. 31 (1998) 107–120, https://doi.org/10.1016/S0301-679X(98)00013-9.

[39] J.-Y. Lee, A.P. Nagalingam, S.H. Yeo, A review on the state-of-the-art of surface finishing processes and related ISO/ASTM standards for metal additive manufactured components, Virtual Phys. Prototyp. 16 (2021) 68–96, https://doi.org/10.1080/17452759.2020.1830346.

[40] E. Maleki, S. Bagherifard, M. Bandini, M. Guagliano, Surface post-treatments for metal additive manufacturing: progress, challenges, and opportunities, Addit. Manuf. 37 (2021), 101619, https://doi.org/10.1016/j.addma.2020.101619.

[41] E. Salerno, D. Casotti, G. Paolicelli, E. Gualtieri, A. Ballestrazzi, G.C. Gazzadi, G. Bolelli, L. Lusvarghi, S. Valeri, A. Rota, Friction and wear of DLC films deposited on additive manufactured AlSi10Mg: the role of surface finishing, Surf. Coat. Technol. 463 (2023), 129531, https://doi.org/10.1016/j.surfcoat.2023.129531.

[42] K.A. Vella, J. Buhagiar, G. Cassar, M.M. Pizzuto, L. Bonnici, J. Chen, X. Zhang, Z. Huang, A. Zammit, The effect of a duplex surface treatment on the corrosion and tribocorrosion characteristics of additively manufactured Ti-6Al-4V, Materials 16 (2023) 2098, https://doi.org/10.3390/ma16052098.

[43] W. Tillmann, N.F. Lopes Dias, D. Stangier, L. Hagen, M. Schaper, F. Hengsbach, K.-P. Hoyer, Tribo-mechanical properties and adhesion behavior of DLC coatings sputtered onto 36NiCrMo16 produced by selective laser melting, Surf. Coat. Technol. 394 (2020), 125748, https://doi.org/10.1016/j.surfcoat.2020.125748.

[44] E. Cerri, E. Ghio, G. Bolelli, Ti6Al4V-ELI alloy manufactured via laser powder-bed fusion and heat-treated below and above the β-Transus: effects of sample thickness and sandblasting post-process, Appl. Sci. 12 (2022) 5359, https://doi.org/10.3390/app12115359.

[45] F. Ahmad, L. Zhang, J. Zheng, I. Sidra, S. Zhang, Characterization of AlCrN and AlCrON coatings deposited on plasma nitrided AISI H13 steels using ion-source-enhanced arc ion plating, Coatings 10 (2020) 306, https://doi.org/10.3390/coatings10040306.

[46] W.Y.H. Liew, J.L.L. Jie, L.Y. Yan, J. Dayou, C.S. Sipaut, M.F. Bin Madlan, Frictional and wear behaviour of AlCrN, TiN, TiAlN single-layer coatings, and TiAlN/AlCrN, AlN/TiN nano-multilayer coatings in dry sliding, Procedia Eng. 68 (2013) 512–517, https://doi.org/10.1016/j.proeng.2013.12.214.

[47] W.Y.H. Liew, S. Dayou, M.A. Bin Ismail, N.J. Siambun, J. Dayou, Dry sliding behaviour of AlCrN and TiN coatings, Adv. Mat. Res. 576 (2012) 559–562, https://doi.org/10.4028/www.scientific.net/AMR.576.559.

[48] Y. Chen, Y.X. Xu, H. Zhang, Q. Wang, T. Wei, F. Zhang, K.H. Kim, Improving high-temperature wear resistance of arc-evaporated AlCrN coatings by Mo alloying, Surf. Coat. Technol. 456 (2023), 129253, https://doi.org/10.1016/j.surfcoat.2023.129253.
[49] E. Cerri, E. Ghio, G. Bolelli, Effect of surface roughness and industrial heat treatments on the microstructure and mechanical properties of Ti6Al4V alloy manufactured by laser powder bed fusion in different built orientations, Mater. Sci. Eng. A 851 (2022), 143635, https://doi.org/10.1016/j.msea.2022.143635.
[50] VDI 3198, in: Verein Deutscher Ingenieure Normen, VDI-Verlag, Düsseldorf, Germany, 1991.
[51] P. Drobný, D. Mercier, V. Koula, S.I. Škrobáková, Ľ. Čaplovič, M. Sahul, Evaluation of adhesion properties of hard coatings by means of indentation and acoustic emission, Coatings 11 (2021) 919, https://doi.org/10.3390/coatings11080919.
[52] Corundum, Aluminum Oxide, Alumina, 99.9%, Al2O3, (n.d.). http://www.matweb.com/search/DataSheet.aspx?MatGUID=c8c56ad547ae4cfabad15977bfb537f1&ckck=1 (accessed September 2, 2017).
[53] S.-J.J. Cho, K.-R.R. Lee, K. Yong Eun, J. Hee Hahn, D.-H.H. Ko, Determination of elastic modulus and Poisson's ratio of diamond-like carbon films, Thin Solid Films 341 (1999) 207–210, https://doi.org/10.1016/S0040-6090(98)01512-0.
[54] K. Komori, N. Umehara, Effect of surface morphology of diamond-like carbon coating on friction, wear behavior and tribo-chemical reactions under engine-oil lubricated condition, Tribol. Int. 84 (2015) 100–109, https://doi.org/10.1016/j.triboint.2014.11.010.
[55] A.C. Ferrari, J. Robertson, Interpretation of Raman spectra of disordered and amorphous carbon, Phys. Rev. B. 61 (2000) 14095–14107, https://doi.org/10.1103/PhysRevB.61.14095.
[56] A.C. Ferrari, Determination of bonding in diamond-like carbon by Raman spectroscopy, Diamond Relat. Mater. 11 (2002) 1053–1061, https://doi.org/10.1016/S0925-9635(01)00730-0.
[57] C. Casiraghi, A.C. Ferrari, J. Robertson, Raman spectroscopy of hydrogenated amorphous carbons, Phys. Rev. B 72 (2005), 085401, https://doi.org/10.1103/PhysRevB.72.085401.
[58] B. Marchon, K. Jing Gui, G.C. Grannen, J.W. Rauch, S.R.P. Ager, J. Robertson Silva, Photoluminescence and Raman spectroscopy in hydrogenated carbon films, IEEE Trans. Magn. 33 (1997) 3148–3150, https://doi.org/10.1109/20.617873.
[59] M. Laurent-Brocq, E. Béjanin, Y. Champion, Influence of roughness and tilt on nanoindentation measurements: a quantitative model, Scanning 37 (2015) 350–360, https://doi.org/10.1002/sca.21220.
[60] A. Anders, A structure zone diagram including plasma-based deposition and ion etching, Thin Solid Films 518 (2010) 4087–4090, https://doi.org/10.1016/j.tsf.2009.10.145.
[61] R. Kaindl, B. Sartory, J. Neidhardt, R. Franz, A. Reiter, P. Polcik, R. Tessadri, C. Mitterer, Semi-quantitative chemical analysis of hard coatings by Raman micro-spectroscopy: the aluminium chromium nitride system as an example, Anal. Bioanal. Chem. 389 (2007) 1569–1576, https://doi.org/10.1007/s00216-007-1540-4.
[62] R. Kaindl, R. Franz, J. Soldan, A. Reiter, P. Polcik, C. Mitterer, B. Sartory, R. Tessadri, M. O'Sullivan, Structural investigations of aluminum-chromium-nitride hard coatings by Raman micro-spectroscopy, Thin Solid Films 515 (2006) 2197–2202, https://doi.org/10.1016/j.tsf.2006.07.144.
[63] J.L. Mo, M.H. Zhu, Sliding tribological behavior of AlCrN coating, Tribol. Int. 41 (2008) 1161–1168, https://doi.org/10.1016/j.triboint.2008.02.007.
[64] M. Antonowicz, R. Kurpanik, W. Walke, M. Basiaga, J. Sondor, Z. Paszenda, Selected physicochemical properties of diamond like carbon (DLC) coating on Ti-13Nb-13Zr alloy used for blood contacting implants, Materials 13 (2020) 5077, https://doi.org/10.3390/ma13225077.
[65] A. Hatem, J. Lin, R. Wei, R.D. Torres, C. Laurindo, P. Soares, Tribocorrosion behavior of DLC-coated Ti-6Al-4V alloy deposited by PIID and PEMS + PIID techniques for biomedical applications, Surf. Coat. Technol. 332 (2017) 223–232, https://doi.org/10.1016/j.surfcoat.2017.07.004.
[66] T.F. Zhang, Q.Y. Deng, B. Liu, B.J. Wu, F.J. Jing, Y.X. Leng, N. Huang, Wear and corrosion properties of diamond like carbon (DLC) coating on stainless steel, CoCrMo and Ti6Al4V substrates, Surf. Coat. Technol. 273 (2015) 12–19, https://doi.org/10.1016/j.surfcoat.2015.03.031.
[67] J.C. Avelar-Batista, E. Spain, G.G. Fuentes, A. Sola, R. Rodriguez, J. Housden, Triode plasma nitriding and PVD coating: a successful pre-treatment combination to improve the wear resistance of DLC coatings on Ti6Al4V alloy, Surf. Coat. Technol. 201 (2006) 4335–4340, https://doi.org/10.1016/j.surfcoat.2006.08.070.
[68] V. Kashyap, P. Ramkumar, DLC coating over pre-oxidized and textured Ti6Al4V for superior adhesion and tribo-performance of hip implant, Surf. Coat. Technol. 440 (2022), 128492, https://doi.org/10.1016/j.surfcoat.2022.128492.
[69] H. Ronkainen, K. Holmberg, Environmental and thermal effects on the tribological performance of DLC coatings, in: C. Donnet, A. Erdemir (Eds.), Tribology of Diamond-like Carbon Films, Springer US, Boston, MA, USA, 2008, pp. 155–200, https://doi.org/10.1007/978-0-387-49891-1_6.
[70] T.W. Scharf, I.L. Singer, Third bodies and tribochemistry of DLC coatings, in: C. Donnet, A. Erdemir (Eds.), Tribology of Diamond-like Carbon Films, Springer US, Boston, MA, USA, 2008, pp. 201–236, https://doi.org/10.1007/978-0-387-49891-1_7.
[71] J.L. Mo, M.H. Zhu, B. Lei, Y.X. Leng, N. Huang, Comparison of tribological behaviours of AlCrN and TiAlN coatings—deposited by physical vapor deposition, Wear 263 (2007) 1423–1429, https://doi.org/10.1016/j.wear.2007.01.051.
[72] M. Gong, J. Chen, X. Deng, S. Wu, Sliding wear behavior of TiAlN and AlCrN coatings on a unique cemented carbide substrate, Int. J. Refract. Met. Hard Mater. 69 (2017) 209–214, https://doi.org/10.1016/j.ijrmhm.2017.08.003.
[73] M. Michalak, R. Michalczewski, E. Osuch-Słomka, D. Maldonado-Cortés, M. Szczerek, The effect of temperature on wear mechanism of the AlCrN coated components, Key Eng. Mater. 674 (2016) 233–238, https://doi.org/10.4028/www.scientific.net/KEM.674.233.
[74] Y.M. Durmaz, F. Yildiz, The wear performance of carbide tools coated with TiAlSiN, AlCrN and TiAlN ceramic films in intelligent machining process, Ceram. Int. 45 (2019) 3839–3848, https://doi.org/10.1016/j.ceramint.2018.11.055.
[75] Titanium Ti-6Al-4V ELI (Grade 23), Annealed, MatWeb Material Property Data. https://www.matweb.com/search/datasheet.aspx?matguid=c4297fb8f1094da189732c224e3be1ed&ckck=1 (accessed July 16, 2023).
[76] J.A. Williams, R.A. Dwyer-Joyce, Contact between solid surfaces, in: B. Bhushan (Ed.), Modern Tribology Handbook Two Volume Set, CRC Press, Boca Raton, FL, USA, 2001, pp. 121–161.
[77] W.M. Rainforth, The wear behaviour of oxide ceramics-a review, J. Mater. Sci. 39 (2004) 6705–6721, https://doi.org/10.1023/B:JMSC.0000045601.49480.79.
[78] G. Straffelini, Friction, in: Friction and Wear - Methodologies for Design and Control, Springer International Publishing, Cham, Switzerland, 2015, pp. 21–60, https://doi.org/10.1007/978-3-319-05894-8_2.
[79] P.S. Souza, A.J. Santos, M.A.P. Cotrim, A.M. Abrão, M.A. Câmara, Analysis of the surface energy interactions in the tribological behavior of AlCrN and TiAlN coatings, Tribol. Int. 146 (2020), 106206, https://doi.org/10.1016/j.triboint.2020.106206.